

Pinv-Recon: Generalized MR Image Reconstruction via Pseudoinversion of the Encoding Matrix

Kylie Yeung^{1,2,3}, Fergus V Gleeson^{2,3}, Rolf F Schulte⁴, Anthony McIntyre³, Sébastien Serres^{5,6}, Peter Morris⁷, Dorothee Auer^{7,8,9}, Damian J Tyler^{1,10,*}, James T Grist^{1,3,10,*}, and Florian Wiesinger^{4,11,*}

¹Oxford Centre for Clinical Magnetic Resonance (OCMR), University of Oxford, Oxford, United Kingdom

²Department of Oncology, University of Oxford, Oxford, United Kingdom

³Department of Radiology, Oxford University Hospitals, Oxford, United Kingdom

⁴GE HealthCare, Munich, Germany

⁵School of Life Sciences, University of Nottingham, Nottingham, UK

⁶The David Greenfield Human Physiology Unit, University of Nottingham, Nottingham, UK

⁷Sir Peter Mansfield Imaging Centre, University of Nottingham, Nottingham, UK

⁸Mental Health and Clinical Neuroscience, School of Medicine, University of Nottingham, Nottingham, UK

⁹NIHR Nottingham Biomedical Research Centre/Nottingham Clinical Research Facilities, QMC, Nottingham, UK

¹⁰Department of Physiology, Anatomy and Genetics, University of Oxford, Oxford, United Kingdom

¹¹Department of Neuroimaging, Institute of Psychiatry, Psychology & Neuroscience, King's College London, London, UK

*These authors contributed equally to this work.

July 2024

A preprint submitted to *Magnetic Resonance in Medicine*.

Corresponding Author: James T Grist, james.grist@cardiov.ox.ac.uk

Keywords: Pinv-Recon, Generalized MR Image Reconstruction, Coil Sensitivity Encoding, B_0 Correction, Chemical Shift Imaging, Hyperpolarized MRI

Abstract

Purpose

To present a novel generalized MR image reconstruction based on pseudoinversion of the encoding matrix (Pinv-Recon) as a simple, versatile, yet powerful method, and demonstrate its computational feasibility for diverse MR imaging applications.

Theory and Methods

MR image encoding constitutes a linear mapping of the unknown image to the measured k-space data mediated via an encoding matrix (**data**=Encode \times **image**). Pinv-Recon addresses MR image reconstruction as a linear inverse problem (**image**=Encode $^{-1}\times$ **data**), explicitly calculating the Moore-Penrose pseudoinverse of the encoding matrix using truncated singular value decomposition (tSVD). Using a discretized, algebraic notation, we demonstrate constructing a generalized encoding matrix by stacking relevant encoding mechanisms (e.g., gradient encoding, coil sensitivity encoding, chemical shift inversion) as well as encoding distortions (e.g., off-center positioning, B_0 inhomogeneity, spatiotemporal gradient imperfections, transient relaxation effects). Iterative reconstructions using the explicit generalized encoding matrix, and the computation of the spatial-response-function (SRF) and noise amplification, were demonstrated.

Results

We evaluated the SVD computation times and memory requirements of Pinv-Recon in dependence of the size of the encoding matrix (time \sim (size of the encoding matrix) $^{1.4}$). Using the Shepp-Logan phantom, we demonstrated the versatility of the method for various intertwined MR image encoding and distortion mechanisms, achieving better MSE, PSNR and SSIM metrics than conventional methods. A diversity of datasets, including the ISMRM CG-SENSE challenge, were used to validate Pinv-Recon.

Conclusion

Although pseudo-inversion of large encoding matrices was once deemed computationally intractable, recent advances make Pinv-Recon feasible. It has great promise for both research and clinical applications, and for educational use.

Keywords: Pinv-Recon, Generalized MR Image Reconstruction, Coil Sensitivity Encoding, B_0 Correction, Chemical Shift Imaging, Hyperpolarized MRI

1 Introduction

MR image encoding is characterized by a linear forward mapping of the unknown image (i.e., the transverse magnetization) to the measured k-space data (i.e., the electrical signals captured by the receiver coils). This linear mapping is typically mediated by an encoding matrix (*Encode*) relating all known or measured k-space data (**data**) to all unknown image voxels (**image**), according to:

$$\mathbf{data} = \mathbf{Encode} \times \mathbf{image} \quad (1)$$

where both **data** and **image** are flattened from multidimensional arrays into 1D vectors. Ideally, the encoding matrix accounts for all relevant desired encoding mechanisms, as well as undesired encoding distortions. Desired encoding mechanisms may include gradient encoding, coil sensitivity encoding, chemical shift encoding, and simultaneous multi-slice encoding; undesired encoding distortions may include B_0 off-resonance, transient relaxation effects, spatiotemporal gradient imperfections, RF transmit inhomogeneity, and spatial off-center positioning. Conventional gradient encoding, for instance, is commonly described by a Fourier matrix (hence also referred to as Fourier encoding: i.e. $\mathbf{Encode} = \mathbf{Gradient} = \exp(j \cdot 2\pi \cdot \mathbf{k} \cdot \mathbf{r})$ with j denoting the imaginary unit, $\mathbf{k} = \gamma \int \mathbf{G} dt$ being the k-space position vector and \mathbf{r} the image space position vector).

When both k-space and image space are sampled on an equidistant Cartesian grid, the forward encoding operation becomes equivalent to the discrete fast Fourier transform (FFT), and correspondingly image reconstruction simplifies to the inverse Fourier transform (iFFT) [1]. Due to its computational efficiency, the FFT algorithm has become the cornerstone of nearly all existing MRI reconstruction algorithms:

$$\mathbf{image} = \mathbf{ImageSpaceProcessing}(\mathbf{iFFT}(\mathbf{kSpaceProcessing}(\mathbf{data}))) \quad (2)$$

typically including pre-FFT k-space processing (e.g., reshaping, interpolation/gridding [2, 3], density compensation, k-space based parallel imaging [4], motion-gating) and post-FFT image domain processing (e.g., reshaping, image-space based parallel imaging, deapodization, gradient non-linearity correction). While extremely efficient, FFT is strictly limited to equidistant Cartesian sampling and is inflexible for non-Cartesian k-space trajectories, varying spatial resolution, non-rectangular image support, complementary encoding mechanisms, and encoding distortions. Such extensions, often encountered in practical MR imaging scenarios, require further consideration and have led to a wide range of specialized reconstruction techniques [5].

Alternatively, MR image reconstruction can be considered as the inverse problem of the linear forward encoding process described in Eq (1) [6, 7]. More specifically, it can be stated as the problem of finding a reconstruction matrix (*Recon*) such as to invert the linear forward encoding. Once the reconstruction matrix is known, MR image reconstruction then simplifies to matrix-vector multiplication, according to:

$$\mathbf{image} = \mathbf{Recon} \times \mathbf{data} \text{ with } \mathbf{Recon} = \mathbf{Encode}^\dagger \quad (3)$$

where \mathbf{Encode}^\dagger indicates the pseudo-inverse of the encoding matrix. While conceptually straightforward and seemingly trivial, direct inversion of the encoding matrix has historically been considered, and is generally still believed to be, computationally intractable [4]. For example, the complex encoding matrix of a 2D 128×128 fully sampled Cartesian MR imaging experiment amounts to $128^2 \times 128^2 = 16384 \times 16384$ corresponding to ~ 2 GB in complex single precision. Although large, the inversion of such matrices is well within reach especially for dedicated image reconstruction computers as commonly found in modern MRI systems, which have 64-bit operating systems, ~ 200 GB RAM and ~ 50 CPU cores. These matrices can even fit into graphics or tensor processing units (GPUs, TPUs) with a large number of parallel processing cores. Importantly, unlike the procedural FFT-based image reconstruction in Eq 2, the Recon matrix in Eq 3 can be calculated from the known encoding during or even before the MR scan, and simply applied to the k-space data once

acquired. Once calculated, the Recon matrix can be used for all subsequent image reconstructions following the same encoding.

This paper aims to demonstrate, for the first time, generalized MR image reconstruction based on pseudoinversion of the encoding matrix, which we refer to as Pinv-Recon. After outlining the algebraic concepts and computational methods, we demonstrate Pinv-Recon for a diverse set of 2D and 3D imaging experiments, including the recent ISMRM CG-SENSE challenge [8]. We exemplify its extreme simplicity, and versatility for handling diverse and intertwined encoding effects, and ability for providing useful image reconstruction metrics related to noise amplification and spatial resolution. In a way, we also intend to herald a turning point away from FFT-based MR image reconstruction, which has served MRI well for nearly 50 years but has also proven inflexible for handling encoding extensions commonly encountered in present-day MR imaging scenarios. To this end, we leverage recent advancements in computing technology, which we anticipate to further continue into the coming years, and reduce MR image reconstruction to its fundamental core of inverting the linear forward encoding by simply computing the pseudoinverse of the encoding matrix.

2 Theory

The following section describes the concept for generalized MR image reconstruction based on pseudoinversion of the encoding matrix, using an algebraic notation inspired by Pruessmann [7]. First, we describe the physics-inspired forward encoding models in a discretized matrix formulation. On the basis of gradient Fourier encoding, we then incrementally add supplementary encoding mechanisms and distortions to form the generalized, discrete forward encoding matrix. Secondly, we introduce the Moore-Penrose pseudoinverse as a versatile method to invert the generalized encoding matrix in both over- and underdetermined image encoding scenarios, and introduce truncated Singular Value Decomposition (tSVD) for efficient computation. Thirdly, we describe extensions of this algebraic formalism for calculating SNR and resolution metrics.

2.1 MR Physics Inspired Forward Encoding

Fourier encoding forms the fundamental basis of spatial localization in most practical MR imaging scenarios [7]. Over the years, it has been complemented by additional encoding mechanisms such as parallel imaging and simultaneous multi-slice imaging based on coil sensitivity [7,9], chemical shift encoding based on variable echo time (TE) readouts [10], amongst others [11–13]. These are described below using a descriptive and self-explanatory notation:

$$\begin{aligned} Gradient_{ik,ir} &= \exp(j \cdot 2\pi \cdot \mathbf{k}_{ik} \cdot \mathbf{r}_{ir}) \\ RxSens_{iRx,ir} &= RxSensMap_{iRx}(\mathbf{r}_{ir}) \\ ChemShift_{iTE,iCS} &= \exp(j \cdot \Delta CS_{iCS} \cdot TE_{iTE}) \end{aligned} \quad (4)$$

where *Gradient* indicates gradient encoding, *RxSens* coil sensitivity encoding based on spatially varying receive coil sensitivity profiles (*RxSensMap*), and *ChemShift* chemical shift (CS) encoding based on variable echo times (TE). The indices *ik*, *ir*, *iRx*, *iCS* and *iTE* number the k-space sampling positions, image-domain voxels, receiver (Rx) coil elements, chemical shift species, and echo times up to *nk*, *nr*, *nRx*, *nCS* and *nTE* respectively.

Besides desired encoding mechanisms, undesired encoding distortions are inevitable in MR imaging and should be accounted for. The most common ones include B_0 off-resonance, relaxation effects, spatio-temporal gradient imperfections [14–18], and spatial off-center positioning:

$$\begin{aligned} OffRes_{ik,ir} &= \exp(j \cdot \Delta B_{0ir} \cdot t_{ik}) \\ Relax_{ik,ir} &= \exp(-R_{ir} \cdot t_{ik}) \end{aligned}$$

Gradient imperfections (*GradNonLin*) : $k_{ik} \rightarrow k'_{ik,ir}$

Spatial off-center positioning (*OffCtr*) : $r_{ir} \rightarrow r_{ir} + \Delta r$ (5)

where $\Delta B_{0,ir}$ indicates the spatially varying B_0 off-resonance, R indicates relaxivity (e.g. $R_2 = 1/T_2$ or $R_{2*} = 1/T_{2*}$), and $k'_{ik,ir}$ indicates the true spatio-temporal encoding field, and Δr indicates the spatial off-center position relative to the gradient iso-center.

Notably, these encoding mechanisms and distortions can be incrementally stacked to form a net encoding matrix of arbitrary complexity, without breaking the linear relationship between the measured data and the unknown image. For example, an experiment with gradient encoding, coil sensitivity encoding and B_0 distortion would result in the following forward encoding model:

$$\mathbf{data}_{ik,iRx} = \text{Encode}_{(ik,iRx),ir} \times \mathbf{image}_{ir}$$

$$\text{Encode}_{(ik,iRx),ir} = \text{Gradient}_{ik,ir} \times \text{RxSens}_{iRx,ir} \times \text{OffRes}_{ik,ir}$$

as illustrated in Figure 1.

Including all the above listed desired encoding mechanisms and undesired distortions, we obtain:

$$\mathbf{data}_{ik,iRx,iTE} = \text{Encode}_{(ik,iRx,iTE),(ir,iCS)} \times \mathbf{image}_{ir,iCS}$$

$$\text{Encode}_{(ik,iRx,iTE),(ir,iCS)} = \text{Gradient}_{ik,ir} \times \text{RxSens}_{iRx,ir} \times \text{ChemShift}_{iTE,iCS} \times \text{OffRes}_{ik,ir} \times \text{Relax}_{ik,ir} \quad (6)$$

with k_{ik} replaced by $k'_{ik,ir}$ and r_{ir} replaced by $r_{ir} + \Delta r$.

2.2 Moore-Penrose Pseudoinverse by Truncated SVD

Pinv-Recon requires inversion of the forward encoding matrix (Eq. 3), which can be accomplished using the Moore-Penrose pseudo-inverse for both overdetermined and underdetermined problems. For over-determined problems (i.e. measurements > unknowns), the Moore-Penrose pseudoinverse provides the least-square solution by solving $\mathbf{image} = \text{argmin}_{\mathbf{image}} \|\text{Encode} \times \mathbf{image} - \mathbf{data}\|^2$, and for under-determined problems it provides the minimum 2-norm solution by solving $\mathbf{image} = \text{argmin}_{\mathbf{image}} \|\mathbf{image}\|^2$ s.t. $\mathbf{data} = \text{Encode} \times \mathbf{image}$.

Several methods exist for computing the Moore-Penrose pseudo-inverse. One approach is to solve the normal equation $\text{Encode}^H \times \mathbf{data} = (\text{Encode}^H \times \text{Encode}) \times \mathbf{image}$ and invert $\text{Encode}^H \times \text{Encode}$. This is employed by conjugate-gradient methods such as CG-SENSE [19], but is known to have poorer conditioning compared to the original Encode matrix and hence may lead to extra noise amplification. Another approach is to decompose Encode , for example by QR decomposition [20] or singular value decomposition (SVD) [21]. Of the two, SVD offers efficient computation and provides robust solutions via truncated SVD (tSVD), according to:

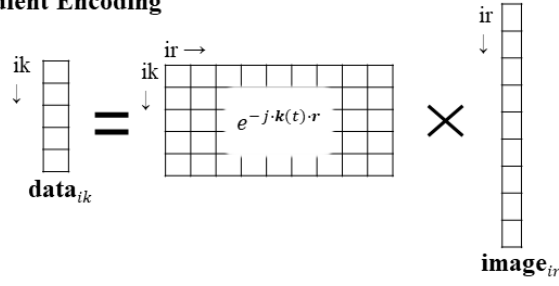
$$\text{Encode} = \mathbf{U} \mathbf{\Sigma} \mathbf{V}^H \quad (7)$$

where $\mathbf{U} \in \mathbb{R}^{ik \times ik}$ and $\mathbf{V} \in \mathbb{R}^{ir \times ir}$ are unitary matrices with orthonormal columns and $\mathbf{\Sigma}$ is a diagonal matrix with the singular values of E. A regularized solution can be obtained by truncating the singular values as follows:

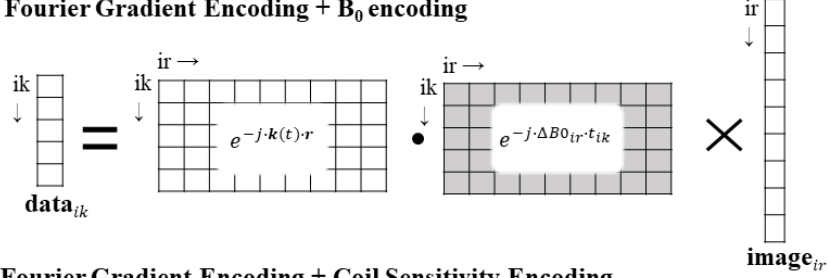
$$\text{Recon} = \tilde{\mathbf{V}} \tilde{\mathbf{\Sigma}}^{-1} \tilde{\mathbf{U}}^H \quad (8)$$

where H denotes the complex conjugate transpose, and $\tilde{\mathbf{U}}, \tilde{\mathbf{\Sigma}}, \tilde{\mathbf{V}}$ denote the truncated matrices. The spectrum of singular values also provides a useful visual impression of the overall conditioning of the Encode matrix via L-curve analysis [22]. Truncated SVD removes singular values below a certain threshold ($t\Sigma$) and thereby provides an efficient and interpretable regularization mechanism. Typically, the truncation threshold is set

Fourier Gradient Encoding



Fourier Gradient Encoding + B_0 encoding



Fourier Gradient Encoding + Coil Sensitivity Encoding

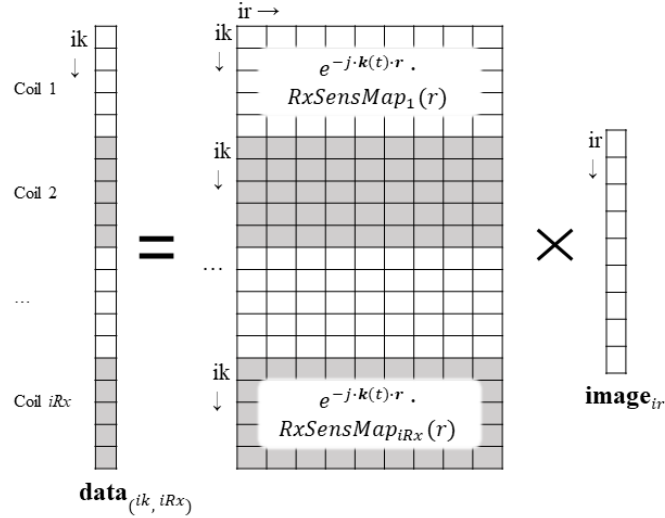


Figure 1: Diagram illustrating the composition and extension of the encoding matrix, top: Fourier Gradient Encoding, middle: Fourier Gradient Encoding with B_0 Encoding, and bottom: Fourier Gradient Encoding with Coil Sensitivity Encoding. \times indicates matrix multiplication, whilst \cdot indicates element-wise multiplication.

to capture a predetermined percentage of the Eigenvalues' cumulative energy (e.g. 95%). The ratio of the largest and the remaining smallest eigenvalue is referred to as the condition number (κ). Adjusting κ effectively serves as a regularization mechanism and allows trading precision versus noise amplification (See Supplementary Material 1). Note that reconstruction matrices with different κ can be realized from the same original untruncated SVD decomposition. Optionally, other regularization methods such as Tikhonov regularization can be used.

For k-space sampling trajectories with arbitrary k-space sampling in the xy-plane and Cartesian phase encoding in z, the reconstruction can be separated into first applying Pinv or iFFT to the z-dimension ($z - Pinv$ or $z - iFFT$), then applying Pinv-Recon as would be done for a 2D trajectory.

Beyond using the encoding matrix alone, including the sample noise matrix $\tilde{\Psi}$ in the calculation of the reconstruction matrix can minimize noise:

$$Recon = (Encode^H \tilde{\Psi}^{-1} Encode)^{-1} Encode^H \tilde{\Psi}^{-1} \quad (9)$$

where $\tilde{\Psi}$ can be derived from the receiver noise matrix Ψ :

$$\tilde{\Psi} = \Psi \otimes Id_m \quad (10)$$

where Id_m is an identity matrix with the size of the number of k-space points and \otimes denotes the Kronecker product [23].

Pseudoinversion of the encoding matrix also enables explicit calculation of derived image metrics related to image noise and resolution [7]. Specifically, the spatial response function (SRF), which is a measure of the proportion of a pixel represented in the reconstructed image, can be calculated from:

$$SRF_{ir,ir'} = \sum_{ik} Recon_{ir,ik} Encode_{ik,ir'} \quad (11)$$

where a value of 1 indicates the signal from that pixel is fully represented in the final image [7]. The noise matrix is given as:

$$X = Recon \tilde{\Psi}^{-1} Recon^H \quad (12)$$

3 Methods

3.1 Algorithmic Considerations and Compute Time

Pinv-Recon offers a uniquely simplistic implementation, especially when taking advantage of numeric computing environments and linear algebra libraries. Such software environments typically offer highly optimized and efficient linear algebra operations and algorithms, such as matrix multiplication, dot product multiplication, SVD, QR, iterative methods for linear systems (e.g., conjugate-gradient or Gauss-Newton solvers), or even methods for calculating the pseudoinverse itself. Many also support multi-threaded and GPU-based operations using different numeric floating-point representations, such as 64-bit double-precision, 32-bit single-precision, and 16-bit half-precision. The following exemplifies 2D Pinv-Recon in MATLAB (MathWorks, Natick, MA) notation for an arbitrary k-space sampling pattern (**kx**, **ky**):

```
Encode=exp(1i*2*pi*(kx(:)*(rx(mask)).'+ky(:)*(ry(mask)).')); % encoding matrix
Recon=pinv(Encode,SVD_threshold); % reconstruction matrix
image=Recon*data; % reconstruction via matrix-vector multiplication
```

where the reconstruction is limited to a spatial mask (**mask**) within the 2D Cartesian grid defined by **rx** and **ry**, and **pinv** calculates the Moore-Penrose pseudoinverse based on tSVD using an optional SVD threshold (cf. Eqs. [7, 8]). MATLAB intrinsically supports multithreading for certain linear algebra and numerical functions (including **pinv** and **svd**) allowing an adjustable number of computational threads (**maxNumCompThreads**). Further computational gains can be obtained using single precision (**single**) and GPU processing (**gpuArray**).

The computational speed was assessed for two different Intel (Santa Clara, CA) CPU configurations, including:

1. Intel® Core™ i9-13950Hx with 24 cores, 32 threads and 64GB RAM
2. Intel® Xeon® Gold 6448: 2 sockets, 32 cores/socket, 2 threads/core and 1TB RAM

and two different NVIDIA (Santa Clara, CA) GPU configurations, including:

1. NVIDIA® RTX 2000 Ada Generation Laptop 8GB
2. NVIDIA® A100 80GB.

All timing calculations were performed using built-in functions (`timeit`, `gputimeit`), measuring the time for SVD (`svd`), which dominates pseudo-inverse calculation, and $Encode^H Encode$ matrix multiplications, which forms the basis of iterative reconstruction methods such as conjugate gradient methods and also serves to illustrate the short time needed for matrix-vector multiplication based image reconstruction. For simplicity, a square encoding matrix was assumed with each dimension being equal to the squared matrix size (i.e., $nr^2 \times nr^2$) and containing complex single precision elements (i.e., `Encode = randn(nr^2, nr^2, 'single') + 1i * randn(nr^2, nr^2, 'single')`). Note that MATLAB's `svd` does not support half-precision, and its GPU arrays indexing is limited to $2^{31} = 2147483647$ elements, corresponding to 8.6GB matrices in single precision.

3.2 Simulation

3.2.1 Fourier Encoding

The versatility of Pinv-Recon for arbitrary k-space sampling patterns was demonstrated using the numerical Shepp-Logan phantom. Commonly used trajectories, including uniform Cartesian, Echo-Planar-Imaging (EPI), two-fold accelerated variable-density Poisson-Disk (VDPD), golden-angle 2D radial, and variable density spiral, were generated for a matrix size 128×128 . A Shepp-Logan phantom was first forward projected into k-space data (Eq. 1, 4), then Pinv-reconstructed (Eq 3) using tSVD (Eq. 7, 8). Unlike in gridding-based methods, no k-space interpolation, density compensation, or deapodization was required [2,3]. Additionally, the spatial response function and the noise matrix were calculated (Eqs. 11, 12).

The reconstruction of spiral trajectories using Pinv-Recon was compared to conventional gridding reconstruction across a range of matrix sizes and SNRs. Further details can be found in the Supplementary Material.

3.2.2 Generalized Encoding

Pinv-Recon is flexible for incorporating multiple encoding mechanisms, as we demonstrate in a 128×128 Shepp-Logan image. Starting with variable-density spiral encoding (*Gradient*), we incrementally add horizontal off-center positioning (*OffCtr*), gradient nonlinearity (*GradNonLin*), off-resonance (*OffRes*), coil sensitivity encoding (*RxSens*) for an acceleration factor of 2×2 , and Dixon-type fat-water chemical shift encoding (*ChemShift*). Note that the 2×2 acceleration introduced as part of *RxSens* shortens the k-space trajectory from 52 ms to 15 ms. Specific details of the simulations can be found in the Git repository provided in the Data Availability Statement. The image was first forward projected using the respective encoding mechanisms, then reconstructed using either a naïve gradient-only encoding matrix spatially discretized relative to the MRI scanner's frame of reference, or a general encoding matrix combining the relevant mechanisms and spatially-discretized relative to the object's frame of reference to correct for off-center positioning.

Pinv-Recon with B_0 modelling included in the encoding matrix was compared to a conventional multi-frequency interpolation (MFI) based B_0 correction method [24], which interpolates the B_0 -corrected image by combining image bins reconstructed at different off-resonant frequencies according to the measured B_0 map. Further details can be found in the Supplementary Material.

3.3 Phantom and In Vivo Validation

Pinv-Recon and its extension to other encoding mechanisms was validated in several datasets, as listed below:

1. Proton
 - (a) 2D-Spiral acquisition of structural phantom and in vivo brain for B_0 correction (2D *Gradient*, *OffRes*)
 - (b) 3D-Stack-of-Stars abdominal scan ($z - iFFT$, 2D *Gradient*)

- (c) 2D-Radial in vivo brain from the recent CG-SENSE reconstruction challenge [8] (2D *Gradient*, *RxSens*)
- 2. Hyperpolarized Xenon-129
 - (a) Stack-of-spirals acquisition of lungs for Pinv-Recon with z-phase encoding (z -*Pinv*, 2D *Gradient*)
 - (b) 2D-Spiral acquisition of lungs for B0 correction (2D *Gradient*, *OffRes*)
- 3. Hyperpolarized Carbon-13
 - (a) 2D-Spiral acquisition of in vivo brain for reconstruction of low SNR data with coil sensitivity encoding (2D *Gradient*, *RxSens*)

Acquisition parameters relevant to the validation of Pinv-Recon are detailed in this section, whilst other specific parameters and acquisition methodology can be found in the Supplementary Material.

3.3.1 Proton

To validate B_0 correction using Pinv-Recon, a structured resolution phantom and a healthy volunteer (Male; Age 30) brain were imaged using single-slice 2D spirals at matrix sizes 48, 64, 96. For each matrix size, a four-arm version with shorter readout was also generated and used as a reference image to determine the accuracy of the B_0 corrected image. The MEDI toolbox [25] was used to fit the B_0 map from varied-TE acquisitions. B_0 correction was implemented in Pinv-Recon by including *OffRes* (Eq. 4), and in gridding reconstruction using MFI with 50 frequency bins [24]. Mean Squared Error (MSE), peak signal-to-noise ratio (PSNR), and structural similarity index measure (SSIM) were computed against the reference image. The study was approved by a local ethics committee (Ref: 20/SC/0441) and the participant provided written informed consent.

To demonstrate Pinv-Recon for large-FOV, high-resolution 3D stack-of-stars encoding, we performed an abdominal, free shallow breathing LAVA-StarTM (GE HealthCare, WI) healthy volunteer scan at a matrix size of $320 \times 320 \times 144$. The data were reconstructed using conventional FFT along the z-phase encoding direction and then Pinv-reconstructed in the xy-plane using varying number of spokes, and varying tSVD threshold. For comparison we also performed a CG-based reconstruction using an explicit encoding matrix and varying number of iterations. In this context, we highlight that the availability of an explicit reconstruction matrix also makes possible real-time imaging by updating the reconstructed image with new incoming spokes (and optionally removing earlier ones) by performing only the relevant fraction of the matrix-vector multiplication-based image reconstruction.

To test Pinv-Recon with coil sensitivity encoding, the 2D radial brain dataset from the ISMRM CG-SENSE challenge was used [8]. This challenge was introduced by the ISMRM reproducible research study group (RRSG) in 2019 where participants aimed to replicate the CG-SENSE algorithm first introduced in Pruessman’s seminal paper [19]. Using Pinv-Recon, acceleration factors of 1,2,3, and 4 were investigated, and compared with the CG-SENSE MATLAB reference implementation using 10 iterations. CG-SENSE addresses sensitivity encoding for arbitrary k-space trajectories by combining gridding principles with CG iterations. The SRF and noise maps were also calculated.

3.3.2 Xenon-129

A stack-of-spirals hyperpolarized Xenon-129 dataset from a healthy volunteer (Female; Age 34) was used to demonstrate Pinv-Recon for non-Cartesian xy-encoding and Cartesian z-phase encoding. Each spiral in the xy-plane had 16 arms and a matrix size of 80×80 . The z axis was sampled with 41 phase encoding steps in a center-out fashion. SNR is quantified, with SNR being defined as the ratio between signal power and noise power.

A low resolution 2D spiral from another volunteer (Female; Age 24) with a longer readout time of 8ms was selected to demonstrate off-resonance distortion correction. The sequence was a single-arm spiral with a 16x16 acquisition matrix and twelve 15 mm slices, which was repeated at different TEs to fit for a B_0 map.

Participants gave informed written consent, and ethics approval was provided by the University of Oxford Central University Research Ethics Approval (Reference: R77150/RE001).

3.3.3 Carbon-13

Sensitivity encoded reconstruction using Pinv-Recon was validated in a hyperpolarized Carbon-13 brain scan (Male; Age 29). The imaging protocol used a spectral-spatial multi-slice single-arm spiral sequence with matrix size 20×20 [26, 27]. Individual coil element sensitivities were calculated from the image of each individual element normalized over the root-sum-of-squares of all coil elements.

Three different coil combination methods were compared, root-sum-of-squares coil combination post-reconstruction, sensitivity-based coil combination post-reconstruction, and coil combination via integrating the coil sensitivity map in Pinv-Recon. In addition, overdiscretized reconstruction was demonstrated. The sample noise matrix was included to optimize SNR (Eq. 9). As this is a relatively low SNR case, the SVD threshold was manually adjusted to 85% of the cumulative energy. For each timestep, the mean SNR was calculated by using a mask of the summed time-series image on Pyruvate to differentiate between signal and noise. This project was approved by the University of Nottingham Medical School Ethics Committee (Ref: 416-1911 BRAIN DNP) and was conducted in accordance with the standards set by the latest version of the Declaration of Helsinki, except for registration in a database. Informed, written consent was obtained from the volunteer beforehand.

4 Results

4.1 Simulations

4.1.1 Computational time

mtx	Size	Memory	time: [U,S,V]=svd(ENCODE)				time: Encode ^H Encode			
			i9	RTX 2000	Xeon	A100	i9	RTX 2000	Xeon	A100
2D: 64x64	4096x4096	134MB	~8s	~7.8s	~3.2s	~6s	~0.5s	~75ms	~70ms	~30ms
2D: 128x128	16384x16384	2.15GB	520s (0:08:30)	~220 (0:03:40)	~200s (0:03:20)	~120s (0:02:00)	~40s	~3s	~4s	~1.9s
2D: 192x192	36864x36864	10.9GB	13800s (3:50:00)	---	~1500s (0:25:00)	~540s (0:09:00)	~550s (0:09:46)	---	~40s	~22s
2D: 256x256	65536x65536	34.36GB	---	---	~9000s (2:30:00)	(*)	---	---	~250s (00:04:10)	(*)
3D: 48x48x48	110592x110592	97.84GB	---	---	~39600s (11:00:00)	---	---	---	~16200s (04:30:00)	---

Table 1: Computational times required for computing the SVD for a range of matrix sizes.

Memory requirements and computational time for different reconstruction matrices are summarized in Table 1. Using high performance computers, similar to those found on modern MR scanners, the compute time required for the inversion of a 2GB encoding matrix is on the order of just a few minutes.

4.1.2 Fourier Encoding

Shepp-Logan phantom simulations demonstrate Pinv-Recon for several commonly used k-space sampling trajectories (Figure 2). The SVD spectra show that Cartesian sampling is the best-conditioned one, as can also

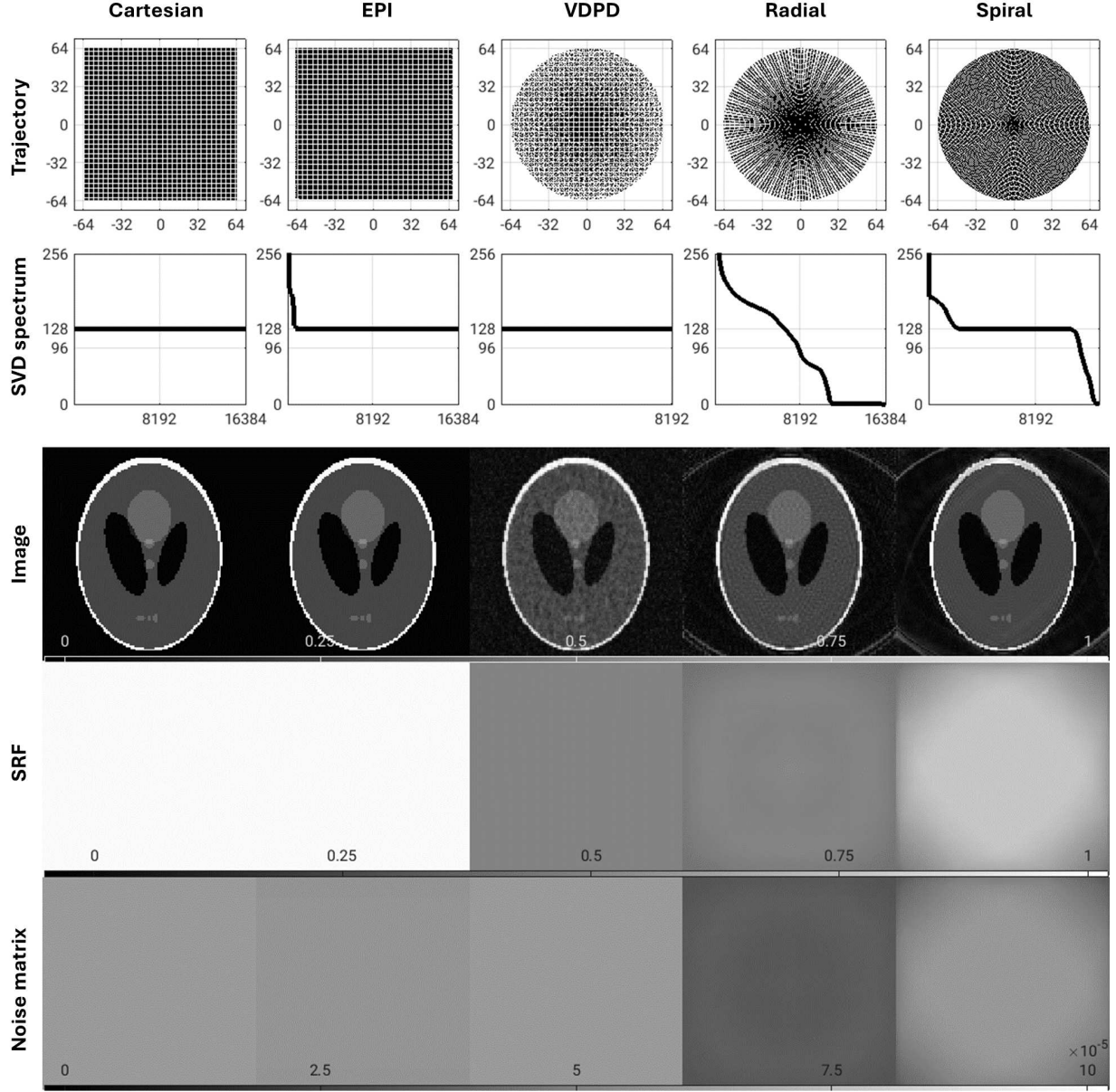


Figure 2: Demonstration of Pinv-Recon on a variety of k-space sampling trajectories. From left to right: Cartesian, EPI, two-fold accelerated Variable-Density Poisson Disk (VDPD), radial, spiral. From top to bottom: sampling trajectory, SVD, reconstructed Shepp-Logan image, SRF, noise matrix.

be appreciated in its artifact-free reconstruction of the Shepp-Logan phantom. Pinv-Recon also allowed the direct calculation of the SRFs, again demonstrating the highest value for fully-sampled Cartesian encoding. The noise matrices reflect spatially dependent noise amplification for the radial and spiral trajectories.

Pinv-Recon results in higher fidelity compared to conventional gridding reconstruction, as on average, Pinv-Recon achieved a 4.6% lower MSE, 4.2% higher PSNR, and 0.5% higher SSIM. An extended analysis can be found in the Supplementary Material.

4.1.3 Generalized Encoding

Shepp-Logan simulations show that intertwined encoding mechanisms can be accounted for in a single general encoding matrix then reconstructed using Pinv-Recon (Figure 3). It can reconstruct the spiral data without requiring gridding, account for off-resonance blurring, remove undersampling artifacts by including coil sensitivity encoding, and separate fat and water signals.

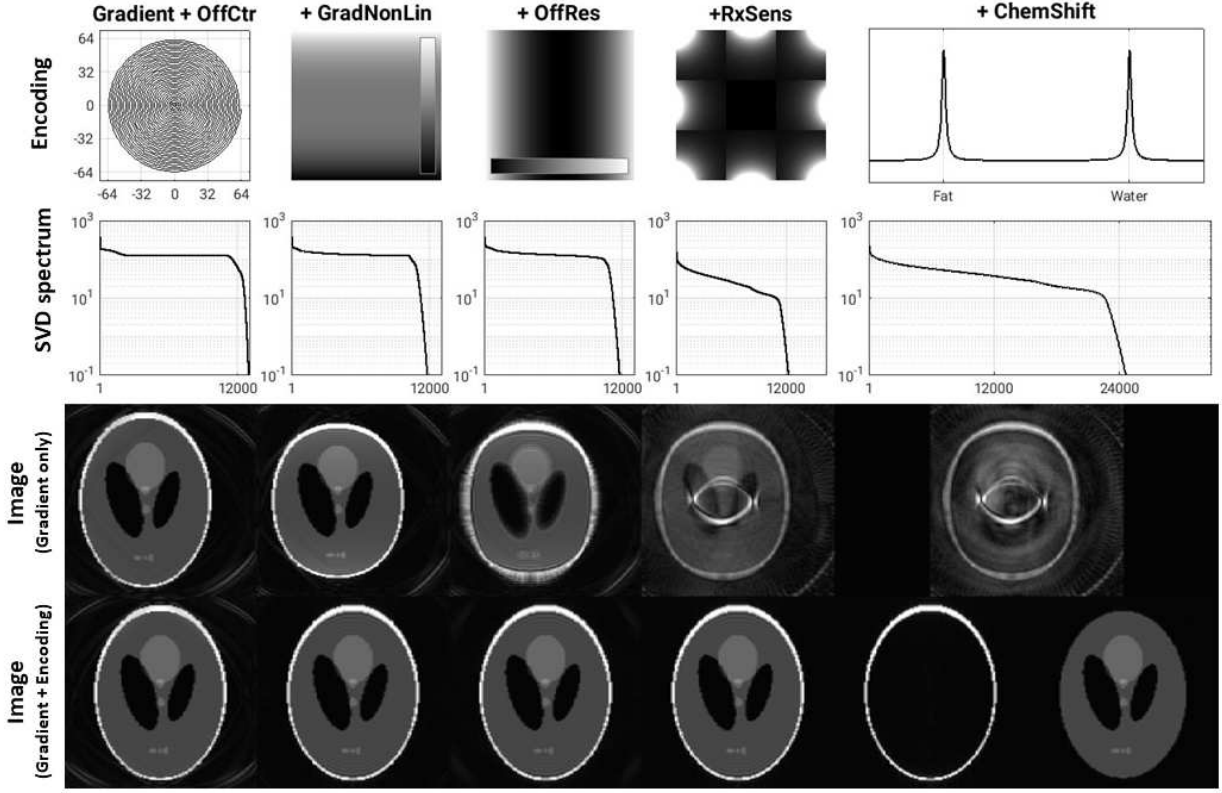


Figure 3: Illustration of Pinv-Recon’s versatility to account for multiple intertwined encoding mechanisms. From top to bottom: illustration of the encoding mechanism, SVD spectrum of general encoding matrix, reconstructed image accounting for gradient encoding only, reconstructed image accounting for all relevant encoding effects. From left to right: spiral gradient encoding + spatial off-center correction, + gradient nonlinearity correction, + B_0 off-resonance, + coil sensitivity encoding, + chemical shift encoding.

Using Pinv-Recon with B_0 correction results in lower MSE, higher PSNR and higher SSIM as compared to using MFI as a B_0 correction method in gridding (Figure 3). Depending on the readout duration and the range of off-resonance frequencies, Pinv-Recon achieves between 31.2% and 75.7% lower MSE, between 7.7% to 29.3% higher PSNR, and between 8.3% to 25.7% higher SSIM. The Supplementary Material contains a more detailed analysis.

4.2 Phantom and In vivo validation

4.2.1 Proton

B_0 correction was validated in a structured resolution phantom at the proton frequency. Off-resonance blurring is present in the single-arm spiral acquisitions (Figure 4). By incorporating the B_0 maps into Pinv-Recon and into an MFI correction for the image obtained through gridding reconstruction, the blurring effects can be ameliorated, recovering images close to the reference image. Pinv-Recon results in lower MSE, higher PSNR, and higher SSIM than MFI for all of the matrix sizes (Table 2). B_0 correction was also validated for an in vivo a human brain scan (Figure 4). Better sharpening can be seen in the images reconstructed using Pinv-Recon with B_0 encoding.

	MTX 48		MTX 64		MTX 96	
	Pinv-Recon	Gridding	Pinv-Recon	Gridding	Pinv-Recon	Gridding
MSE	0.001343	0.001667	0.000971	0.001736	0.000877	0.002350
PSNR	28.72	27.78	30.12	27.60	30.57	26.29
SSIM	0.8194	0.7859	0.8206	0.7815	0.8465	0.7670

Table 2: Results comparing B_0 correction using Pinv-Recon versus using gridding with MFI correction in a structured resolution phantom.

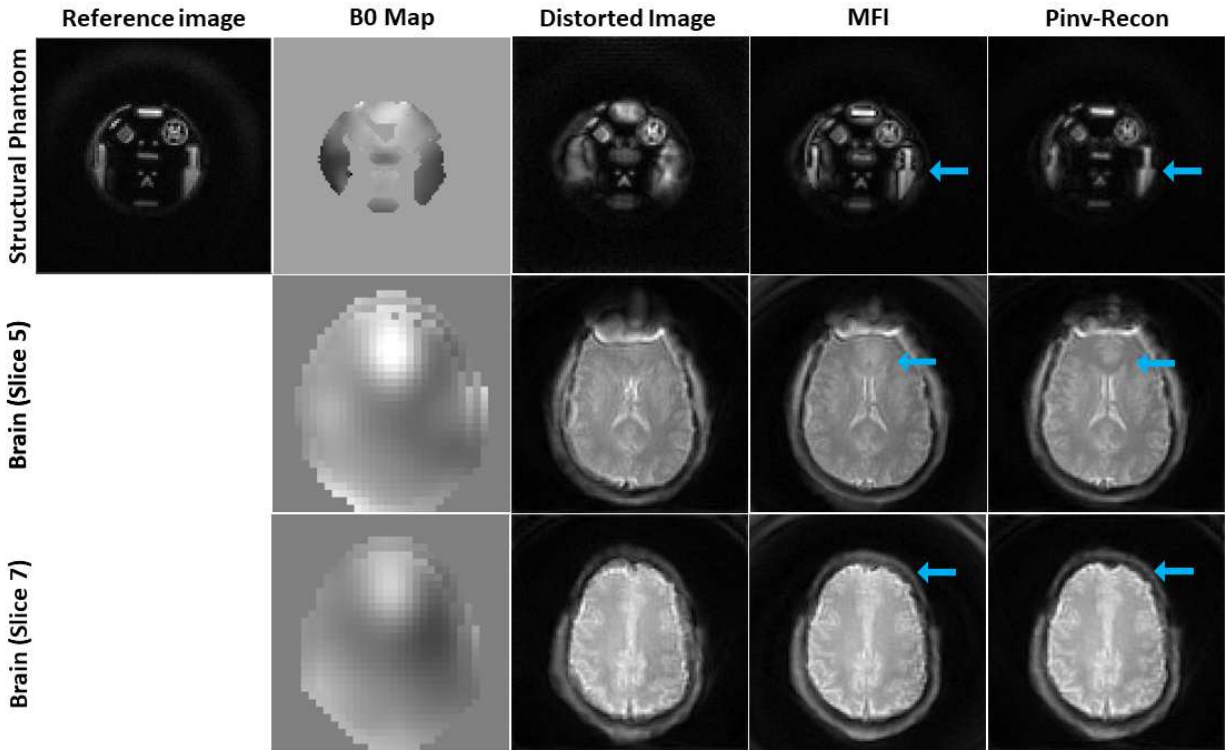


Figure 4: Comparison of MFI versus Pinv-Recon in the correction of off-resonance distortion in proton phantom and in vivo images. From top to bottom: phantom dataset, slice 5 of brain dataset, slice 7 of brain dataset. From Left to right: reference short readout time image, B_0 map, B_0 distorted image, gridding reconstructed image with MFI correction, and Pinv-Recon image with incorporated B_0 correction. Areas with distinctive differences in the two correction methods are emphasized with the blue arrow.

Figure 5 illustrates Pinv-reconstructed 3D large-FOV, high-resolution, abdominal LAVA-Star images using stack-of-stars based image encoding. The top row shows images obtained using fractions of the available spokes, indicating smooth convergence and demonstrating its potential for real-time imaging. The middle row shows images obtained using varying thresholds for the tSVD based calculation of the reconstruction matrix, demonstrating the trade-off between resolution and SNR offered by varying the condition number κ , also illustrated in the SVD spectrum on the right. The bottom row shows images reconstructed using the iterative CG algorithm with explicit matrix vector multiplications. As is common with CG-based iterative methods, image quality first improves, peaks and then degrades with increasing number of iterations.

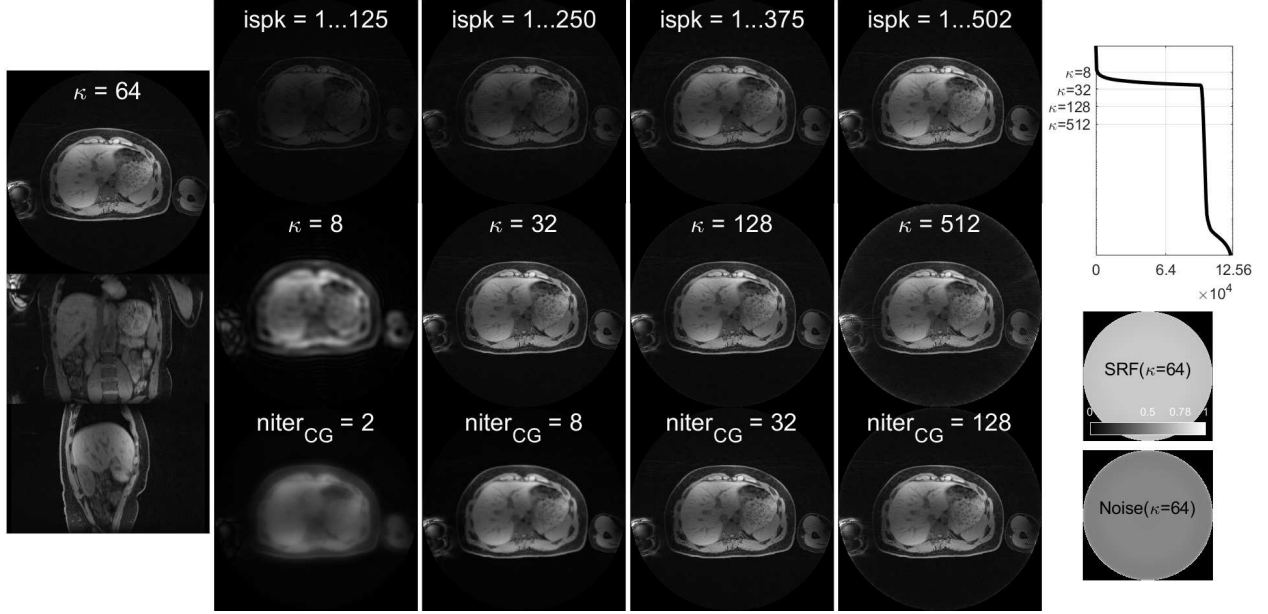


Figure 5: Left: Axial, coronal and sagittal views of the 3D dataset. In the middle four columns, top: varying the number of spokes used in reconstruction, middle: varying the condition number κ by changing the tSVD threshold, bottom: varying the number of iterations in images reconstructed using CG with explicit matrix vector multiplications. Right: SVD spectrum, SRF map, and noise map.

Reconstruction of undersampled datasets using coil sensitivity encoding was demonstrated using the ISMRM CG-SENSE challenge dataset. Streaking artifacts characteristic of undersampled radial data are present in the data reconstructed using CG-SENSE, whereas these streaking artifacts are largely removed in Pinv-Recon with coil sensitivity encoding (Figure 6). The image noise and SRF maps illustrate spatially varying resolution and noise which both worsen at higher acceleration factors.

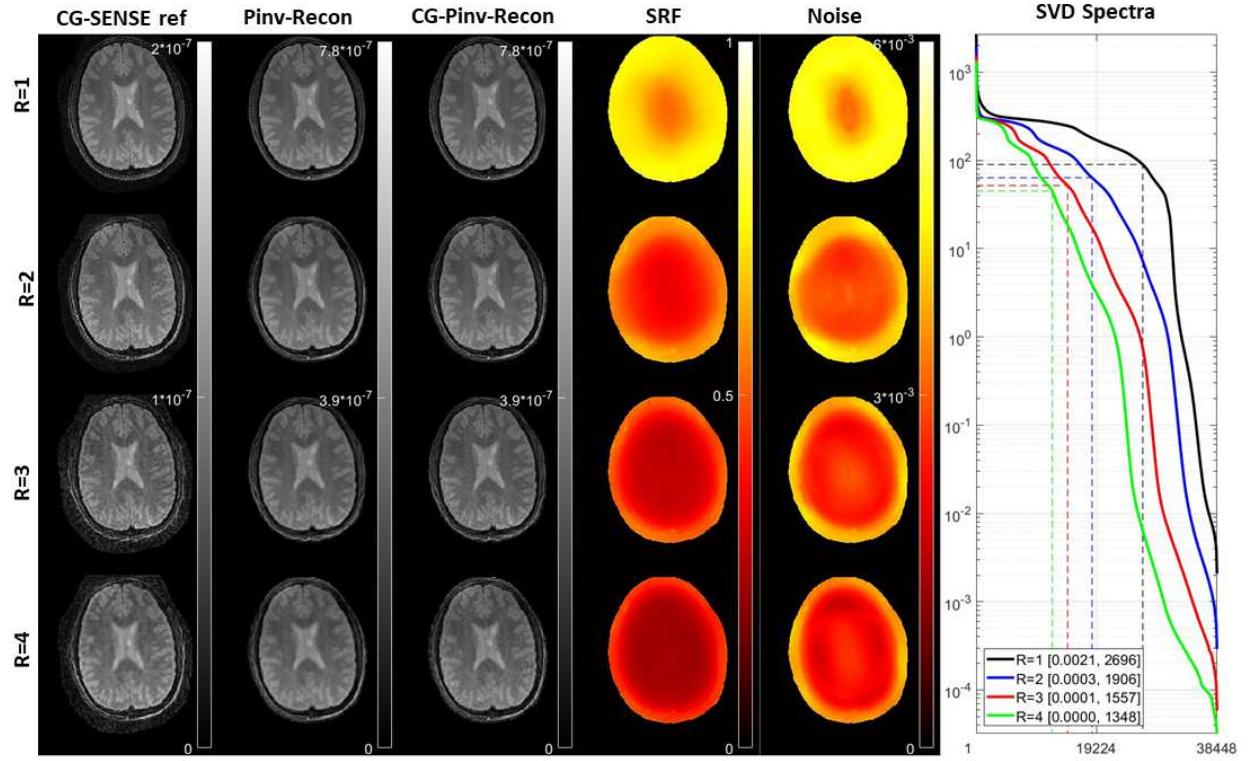


Figure 6: Top to bottom: Acceleration factors of 1 to 4. Left to right: Reconstruction using ISMRM CG-SENSE reference implementation in MATLAB, reconstruction using Pinv-Recon with coil sensitivity encoding, reconstruction using iterative CG with an explicit encoding matrix, SRF, noise map, SVD spectra.

4.2.2 Xenon-129

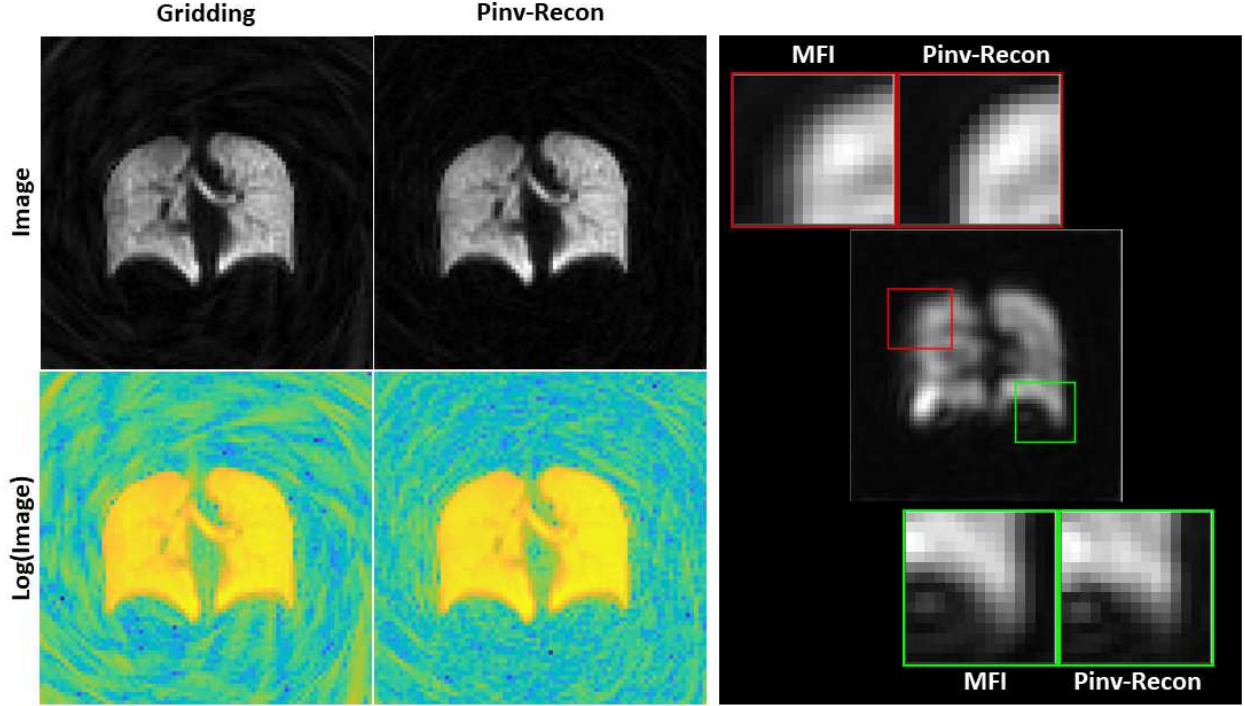


Figure 7: Left: Reconstruction of stack-of-spirals data using gridding results in streaking artifacts, whilst Pinv-Recon eliminates these artifacts and boosts SNR, shown in original scale (top), and log scale (bottom). Right: Comparison of B_0 correction using MFI versus Pinv-Recon, with the original uncorrected image shown in the center and corrected regions-of-interest comparing both methods shown on top and bottom.

Reconstruction of a stack-of-spirals trajectory was demonstrated in a hyperpolarized Xenon-129 dataset. For this matrix size (80×80 in xy-plane and 41 in the z-axis), reconstruction of the entire volume took ~ 15 seconds. With a pre-calculated reconstruction matrix, the image can be reconstructed in 0.026s, whilst gridding takes 0.16s. Streaking artifacts present in the gridding reconstructed image are not seen in the image reconstructed using Pinv-Recon, and SNR is improved by 75.3%.

B_0 correction was demonstrated in a lower resolution 2D spiral dataset, which had a longer readout time. Off-resonance blurring can be observed in the original image. Using gridding reconstruction with MFI correction and using Pinv-Recon with embedded B_0 encoding improved image quality, but Pinv-Recon sharpens the image to a greater extent.

4.2.3 Carbon-13

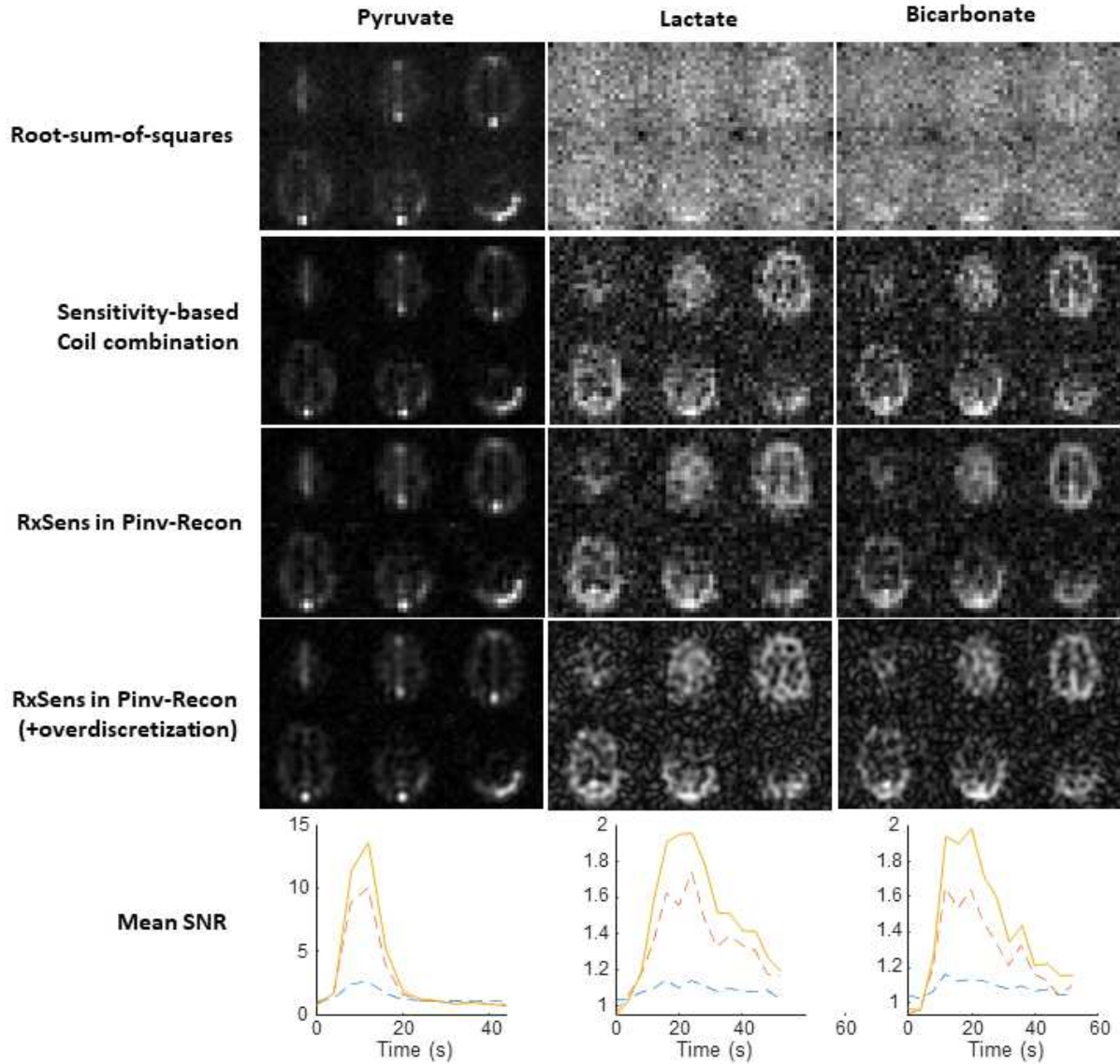


Figure 8: Comparison of different coil combination approaches in Pinv-Recon on multichannel hyperpolarized carbon-13 data. From left to right: Pyruvate, Lactate, Bicarbonate. From top to bottom: root-sum-of-squares coil combination, sensitivity-based coil combination, Pinv-Recon with coil sensitivity map included, Pinv-Recon with coil sensitivity map included reconstructed to an overdiscretized spatial grid (64×64). Mean SNR values for the first three methods are plotted in the bottom row in dotted blue, dotted red, and yellow respectively.

SNR improvement was demonstrated in a low SNR hyperpolarized carbon-13 dataset using Pinv-Recon with coil sensitivity encoding. Although straightforward, the root-sum-of-squares coil combination approach is suboptimal for low SNR datasets. SNR was improved by calibration-based coil combination, and further enhanced by the inclusion of the coil-sensitivity map in Pinv-Recon. Since the coil sensitivity is spatially-varying but time invariant, the reconstruction matrix has to be calculated for each individual slice, but can be reused for each time point and metabolite. Calculation of the reconstruction matrices for 8 slices was 0.3872 seconds in total. Averaged over the time course, using Pinv-Recon increased the mean SNR by 10.6%, 10.1%, and 11.4% for pyruvate, lactate and bicarbonate respectively. Overdiscretized reconstruction from a matrix size of 20×20 to 64×64 was also demonstrated.

5 Discussion

Pinv-Recon, previously considered prohibitive due to its high computational demands, is shown here to not only be feasible, but also advantageous over conventional image reconstruction pipelines because it circumvents the limitations of the FFT and allows the integration of multiple intertwined encoding mechanisms in a very flexible and general manner.

Computational intensiveness is the primary reason the Pinv reconstruction approach has not been adopted or even considered in the past few decades. However, with the drastic increase in computational power [28] and the development of advanced processors and software, inverting large matrices is now much more feasible and efficient. In principle, modern 64-bit operating systems allow addressing 16EB (Exabyte) memory, far exceeding the 4GB limitation of 32-bit systems [29]. While 64-bit processors have existed since the 1980s, widespread support in drivers and software only became available in the last decade. For instance, MATLAB became compatible with 64-bit systems in 2004 for Linux and Windows, and in 2009 for Mac [30,31]. Modern day clinical MRI reconstruction hardware, with ~ 200 GB RAM and ~ 50 CPU cores, can perform operations in seconds that once took hours [32]. Taking the $80 \times 80 \times 41$ hyperpolarized Xenon-129 stack-of-spirals dataset for example, the encoding matrices (11776×6400 in xy and 41×41 in z) can be pseudo-inverted in ~ 15 s and the reconstructed image can then be obtained in as little as 0.03s. From a clinical application perspective, Pinv-Recon can be very fast because the encoding matrix can be inverted beforehand, and only needs to be inverted once for a given k-space sampling pattern. Alternatively, when the reconstruction matrix has experimental or patient dependencies (e.g. coil sensitivity, B_0 maps, spatiotemporal gradient imperfections), the inversion can be initiated at the beginning of the acquisition, and as soon as the scanning is finished, only a simple and fast matrix multiplication remains. For chemical shift imaging applications such as a hyperpolarized Carbon-13 dataset with a matrix size of 16×16 with 8 slices, Pinv-Recon with coil sensitivity encoding takes under a second and can be applied to each repetition.

The simplicity of Pinv-Recon has advantages beyond reconstructing more accurate images. From an implementation perspective, applying Pinv-Recon with different encoding mechanisms makes debugging much less cumbersome than implementing multiple layers of correction algorithms. This is also beneficial from a reproducibility standpoint, because it has been noted that deviations in algorithmic details can lead to strong differences in results [8]. Researchers developing novel reconstruction techniques may also use Pinv-Recon as a reference reconstruction method since it provides the generic linear-least squares solution or the minimum 2-norm solution for underdetermined cases. Moreover, Pinv-Recon can be used as an instructive educational tool for students familiarizing themselves with various aspects of MR physics, because its modularity enables each encoding mechanism to be separately visualized (c.f. Figures 2, 3).

For decades, the FFT algorithm has served the MRI field well and enabled MRI to become clinically feasible. However, many complexities had to be introduced to accommodate its use, in particular for non-uniform sampling. Pinv-Recon removes the need for pre-FFT gridding algorithms which interpolate data points and inadvertently distort the data, and for density compensation functions associated with varying k-space sampling density, the calculation of which can be computationally expensive [2, 33]. Pinv-Recon also allows the reconstruction of non-Cartesian data onto an over-discretized spatial grid, which effectively allows spatial refinement in an optimal least-square or minimum 2-norm manner based on the encoding matrix [34]. Unlike gridding, Pinv-Recon does not require density compensation, deapodization, off-center frequency modulation, half-voxel shifts, field-of-view adjustments, and so on. Simulations show Pinv-Recon’s increased accuracy for non-Cartesian trajectories, and hyperpolarized ^{129}Xe data demonstrated significant image quality improvements by eliminating gridding artifacts.

Furthermore, k-space and image-space post-processing algorithms associated with the FFT can also be replaced by simple integration of their encoding mechanisms into the reconstruction matrix. In numerical simulations, we demonstrated the extensive capabilities of Pinv-Recon to include off-center reconstruction, B_0 off-resonance correction, gradient nonlinearity correction, coil sensitivity encoding, and chemical shift

encoding. Pinv-Recon offers a direct solution rather than an iterative approach to these encoding mechanisms [35–37], and allows them to be integrated in one reconstruction step rather than using multiple separate correction algorithms. To the best of our knowledge, no existing reconstruction method allows this level of flexibility, especially not for non-Cartesian sampling trajectories.

This work focused on validating integrated B_0 correction and coil sensitivity encoding across a diverse range of phantom and in vivo datasets. Pinv-Recon further sharpened images with off-resonance distortion based on a continuous B_0 off-resonance spectrum rather than discretizing it to a few discrete bins, as is done in current interpolatory methods. Correction with Pinv-Recon handles large off-resonances better because its accuracy does not depend on the density of pre-selected off-resonance frequencies. Pinv-Recon also simplified parallel imaging reconstruction, especially for non-Cartesian trajectories, and offered improved performance. Present non-Cartesian parallel imaging algorithms are non-trivial and significantly different from Cartesian parallel imaging techniques to accommodate the complex aliasing structure intrinsic to non-Cartesian trajectories [4]. Using Pinv-Recon, coil sensitivity can be included in the reconstruction matrix, allowing the unfolding problem in undersampled data to be directly solved. For fully-sampled data, including coil sensitivity can boost SNR by optimizing coil combination, especially useful for low SNR applications such as hyperpolarized Carbon-13 [38].

Explicit inversion of the encoding matrix, which has generally been avoided in current reconstruction methods, also has advantages of its own. For instance, the SRF and the noise matrices can be explicitly calculated and incorporated in cost-functions for deep-learning based applications. The noise matrix can also be used to analyze noise amplification, similar to the g-factor in parallel imaging reconstructions, as well as for quality assurance and system calibration [39–43]. Moreover, the SVD spectrum of the encoding matrix, the SRF and the noise matrices can be used to optimize image encoding strategies.

Pinv-Recon has become feasible for many imaging contexts, as MRI dataset sizes have grown moderately due to acquisition and physiological factors. It is particularly suited for imaging with small to medium-sized matrix sizes (256×256 or smaller). Several novel MRI techniques, such as hyperpolarized MRI [44], diffusion [45], functional imaging (fMRI, ASL) [46, 47], multinuclear spectroscopy (MNS) [48], and low field imaging [49], focus on generating physiologically relevant contrasts. These methods often have low SNR, benefit from lower spatial resolution and shorter readout times of non-Cartesian trajectories, but on the other hand are often affected by encoding distortions related to gradient nonlinearities and B_0 inhomogeneity. This is particularly true for low field MR imaging.

Pinv-Recon requires regularization by thresholding small singular values, which limits noise amplification but also introduces variability. For simplicity, this work truncates the SVD at 95% of cumulative energy, offering improved reconstruction compared to traditional gridding methods. However, low SNR applications may benefit from a higher threshold. Future work could explore automatic determination of optimal SVD thresholds based on encoding characteristics such as the SVD spectrum and noise levels, or even soft thresholding. Extensive literature exists on optimal SVD threshold selection [50], which potentially can be translated to Pinv-Recon.

Some previous works allude to MR image reconstruction via explicit formulation of the encoding matrix and/or calculating its pseudoinverse, from the perspectives of viewing image reconstruction as a discrete-to-continuous mapping problem [32], minimum-norm SENSE spectroscopic imaging [51], and using the explicit encoding matrix for higher-order reconstruction in the presence of spatiotemporal field perturbations [52]. While related, to the best of our knowledge, the present work is novel by formalizing the inclusion of multiple intertwined encoding mechanisms and validating Pinv-Recon as a method across a diverse range of datasets.

Many computational developments on the horizon also promise to further accelerate the inversion of encoding matrices and make Pinv-Recon feasible for even larger matrix sizes. Amongst them, NVIDIA is about to introduce a new 384GB memory GPU (GB200 Blackwell GPU) and a liquid-cooled, rack-scale exacomputer connecting 32CPUs and 72GPUs (GB200 NVL72). Similarly, Cerebras’ (Sunnyvale, CA) wafer-scale technology enables high-performance computing with 900,000 cores and 44GB memory on a single

chip [53]. While not yet supported by the `svd` function in MATLAB, 16bit half-precision floating point operations are already available in TensorFlow and Pytorch via CUDA/NVIDIA, offering opportunities to further accelerate the large matrix operations intrinsic to Pinv-Recon.

6 Conclusion

This work challenges the presumption that image reconstruction with the pseudoinverse of the encoding matrix is computationally intractable, and reframes the MRI reconstruction approach from a multi-step process centered around the FFT, to a straightforward matrix inversion incorporating various encoding mechanisms, whether desired or undesired. Its generality and simplicity makes it accurate, efficient, and highly versatile, proving advantageous over current image reconstruction pipelines involving gridding reconstruction and interpolation-based or iterative algorithms. The viability and advantages of Pinv-Recon were validated across numerical phantom simulations, physical phantoms, and in vivo datasets of different organs and nuclei. This work demonstrated reduction of gridding artifacts, improved B_0 correction and simplified coil sensitivity encoding, but the capabilities of Pinv-Recon extend far beyond the scope this work. We anticipate Pinv-Recon to revolutionize the approach to MR image reconstruction and also to be made more efficient with the continual advancement of compute hardware and software.

7 Data Availability Statement

The code supporting the numerical simulations in this manuscript, as well as some example datasets can be found at <https://github.com/univ39/Pinv-Recon>.

8 Acknowledgements

KY acknowledges an Oxford-Medical Research Council Doctoral Training Partnership iCASE award, the Oxford-Radcliffe Scholarship, and GE HealthCare for graduate funding. DJT was funded by a British Heart Foundation Senior Basic Science Research Fellowship (FS/19/18/34252). JTG is funded by the Oxford Biomedical Research Centre, and also acknowledges the BHF Centre of Research Excellence, University of Oxford for funding. The proton datasets were funded by the Oxford NIHR Biomedical Research Centre (NIHR203311), the hyperpolarized Xenon-129 datasets were funded by the British Heart Foundation (RE/18/3/34214) and the hyperpolarized Carbon-13 dataset was funded by Nottingham Life cycle 5.

9 Conflict of interest statement

RFS and FW are employees of GE HealthCare.

References

- [1] James W. Cooley and John W. Tukey. An Algorithm for the Machine Calculation of Complex Fourier Series. *Mathematics of Computation*, 19(90):297–301, 1965. Publisher: American Mathematical Society.
- [2] V. Rasche, R. Proksa, R. Sinkus, P. Börnert, and H. Eggers. Resampling of data between arbitrary grids using convolution interpolation. *IEEE transactions on medical imaging*, 18(5):385–392, May 1999.
- [3] Philip J. Beatty, Dwight G. Nishimura, and John M. Pauly. Rapid gridding reconstruction with a minimal oversampling ratio. *IEEE transactions on medical imaging*, 24(6):799–808, June 2005.

- [4] Katherine L. Wright, Jesse I. Hamilton, Mark A. Griswold, Vikas Gulani, and Nicole Seiberlich. Non-Cartesian parallel imaging reconstruction. *Journal of Magnetic Resonance Imaging*, 40(5):1022–1040, 2014.
- [5] Mehmet Akcakaya, Mariya Ivanova Doneva, and Claudia Prieto. *Magnetic Resonance Image Reconstruction*. November 2022.
- [6] Gastao Cruz, Burhaneddin Yaman, Mehmet Akçakaya, Mariya Doneva, and Claudia Prieto. Chapter 2 - MRI Reconstruction as an Inverse Problem. In Mehmet Akçakaya, Mariya Doneva, and Claudia Prieto, editors, *Advances in Magnetic Resonance Technology and Applications*, volume 7 of *Magnetic Resonance Image Reconstruction*, pages 37–57. Academic Press, January 2022.
- [7] Klaas P. Pruessmann. Encoding and reconstruction in parallel MRI. *NMR in biomedicine*, 19(3):288–299, May 2006.
- [8] Oliver Maier, Steven Hubert Baete, Alexander Fyrdahl, Kerstin Hammernik, Seb Harreveld, Lars Kasper, Agah Karakuzu, Michael Loecher, Franz Patzig, Ye Tian, Ke Wang, Daniel Gallichan, Martin Uecker, and Florian Knoll. CG-SENSE revisited: Results from the first ISMRM reproducibility challenge. *Magnetic Resonance in Medicine*, 85(4):1821–1839, 2021. [_eprint: https://onlinelibrary.wiley.com/doi/pdf/10.1002/mrm.28569](https://onlinelibrary.wiley.com/doi/pdf/10.1002/mrm.28569).
- [9] David J. Larkman, Joseph V. Hajnal, Amy H. Herlihy, Glyn A. Coutts, Ian R. Young, and Gosta Ehnholm. Use of multicoil arrays for separation of signal from multiple slices simultaneously excited. *Journal of magnetic resonance imaging: JMRI*, 13(2):313–317, February 2001.
- [10] Florian Wiesinger, Eliane Weidl, Marion I. Menzel, Martin A. Janich, Oleksandr Khagai, Steffen J. Glaser, Axel Haase, Markus Schwaiger, and Rolf F. Schulte. IDEAL spiral CSI for dynamic metabolic MR imaging of hyperpolarized [1-13C]pyruvate. *Magnetic Resonance in Medicine*, 68(1):8–16, 2012. [_eprint: https://onlinelibrary.wiley.com/doi/pdf/10.1002/mrm.23212](https://onlinelibrary.wiley.com/doi/pdf/10.1002/mrm.23212).
- [11] D. I Hoult. Rotating frame zeugmatography. *Journal of Magnetic Resonance (1969)*, 33(1):183–197, January 1979.
- [12] A. A. Maudsley. Fourier imaging using rf phase encoding. *Magnetic Resonance in Medicine*, 3(5):768–777, 1986. [_eprint: https://onlinelibrary.wiley.com/doi/pdf/10.1002/mrm.1910030512](https://onlinelibrary.wiley.com/doi/pdf/10.1002/mrm.1910030512).
- [13] Ralf Kartäusch, Toni Driessle, Thomas Kampf, Thomas Christian Basse-Lüsebrink, Uvo Christoph Hoelscher, Peter Michael Jakob, Florian Fidler, and Xavier Helluy. Spatial phase encoding exploiting the Bloch–Siegert shift effect. *Magnetic Resonance Materials in Physics, Biology and Medicine*, 27(5):363–371, October 2014.
- [14] J. H. Duyn, Y. Yang, J. A. Frank, and J. W. van der Veen. Simple correction method for k-space trajectory deviations in MRI. *Journal of Magnetic Resonance (San Diego, Calif.: 1997)*, 132(1):150–153, May 1998.
- [15] Christoph Barmet, Nicola De Zanche, and Klaas P. Pruessmann. Spatiotemporal magnetic field monitoring for MR. *Magnetic Resonance in Medicine*, 60(1):187–197, July 2008.
- [16] Pekka Sipilä, Sebastian Greding, Gerhard Wachutka, and Florian Wiesinger. 2H transmit–receive NMR probes for magnetic field monitoring in MRI. *Magnetic Resonance in Medicine*, 65(5):1498–1506, 2011. [_eprint: https://onlinelibrary.wiley.com/doi/pdf/10.1002/mrm.22741](https://onlinelibrary.wiley.com/doi/pdf/10.1002/mrm.22741).
- [17] Nii Okai Addy, Holden H. Wu, and Dwight G. Nishimura. Simple method for MR gradient system characterization and k-space trajectory estimation. *Magnetic Resonance in Medicine*, 68(1):120–129, July 2012.

- [18] Jürgen Rahmer, Peter Mazurkewitz, Peter Börnert, and Tim Nielsen. Rapid acquisition of the 3D MRI gradient impulse response function using a simple phantom measurement. *Magnetic Resonance in Medicine*, 82(6):2146–2159, 2019. [.eprint: https://onlinelibrary.wiley.com/doi/pdf/10.1002/mrm.27902](https://onlinelibrary.wiley.com/doi/pdf/10.1002/mrm.27902).
- [19] Klaas P. Pruessmann, Markus Weiger, Peter Börnert, and Peter Boesiger. Advances in sensitivity encoding with arbitrary k-space trajectories. *Magnetic Resonance in Medicine*, 46(4):638–651, 2001. [.eprint: https://onlinelibrary.wiley.com/doi/pdf/10.1002/mrm.1241](https://onlinelibrary.wiley.com/doi/pdf/10.1002/mrm.1241).
- [20] Walter Gander. Algorithms for the QR decomposition. *Res. Rep.*, 80(02):1251–1268, 1980.
- [21] Singular Value Decomposition (SVD). In J. Nathan Kutz and Steven L. Brunton, editors, *Data-Driven Science and Engineering: Machine Learning, Dynamical Systems, and Control*, pages 3–46. Cambridge University Press, Cambridge, 2019.
- [22] Per C. Hansen and Dianne P. O’Leary. The Use of the L-Curve in the Regularization of Discrete Ill-Posed Problems | SIAM Journal on Scientific Computing. *SIAM Journal on Scientific Computing*, 14(6):1487–1503, 1993.
- [23] K. P. Pruessmann, M. Weiger, M. B. Scheidegger, and P. Boesiger. SENSE: sensitivity encoding for fast MRI. *Magnetic Resonance in Medicine*, 42(5):952–962, November 1999.
- [24] Lai-Chee Man, John M. Pauly, and Albert Macovski. Multifrequency interpolation for fast off-resonance correction. *Magnetic Resonance in Medicine*, 37(5):785–792, 1997. [.eprint: https://onlinelibrary.wiley.com/doi/pdf/10.1002/mrm.1910370523](https://onlinelibrary.wiley.com/doi/pdf/10.1002/mrm.1910370523).
- [25] Ludovic de Rochefort, Ryan Brown, Martin R. Prince, and Yi Wang. Quantitative MR susceptibility mapping using piece-wise constant regularized inversion of the magnetic field. *Magnetic Resonance in Medicine*, 60(4):1003–1009, 2008. [.eprint: https://onlinelibrary.wiley.com/doi/pdf/10.1002/mrm.21710](https://onlinelibrary.wiley.com/doi/pdf/10.1002/mrm.21710).
- [26] James T. Grist, Esben S.S. Hansen, Juan D. Sánchez-Heredia, Mary A. McLean, Rasmus Tougaard, Frank Riemer, Rolf F. Schulte, Joshua D. Kaggie, Jan Henrik Ardenkjaer-Larsen, Christoffer Laustsen, and Ferdia A. Gallagher. Creating a clinical platform for carbon-13 studies using the sodium-23 and proton resonances. *Magnetic Resonance in Medicine*, 84(4):1817–1827, 2020. [.eprint: https://onlinelibrary.wiley.com/doi/pdf/10.1002/mrm.28238](https://onlinelibrary.wiley.com/doi/pdf/10.1002/mrm.28238).
- [27] Rolf F. Schulte, Jonathan I. Sperl, Eliane Weidl, Marion I. Menzel, Martin A. Janich, Oleksandr Khegai, Markus Durst, Jan Henrik Ardenkjaer-Larsen, Steffen J. Glaser, Axel Haase, Markus Schwaiger, and Florian Wiesinger. Saturation-recovery metabolic-exchange rate imaging with hyperpolarized [1-13C] pyruvate using spectral-spatial excitation. *Magnetic Resonance in Medicine*, 69(5):1209–1216, 2013. [.eprint: https://onlinelibrary.wiley.com/doi/pdf/10.1002/mrm.24353](https://onlinelibrary.wiley.com/doi/pdf/10.1002/mrm.24353).
- [28] GE Moore. Cramming More Components onto Integrated Circuits. *Electronics*, 38(8):1–14, 1965.
- [29] Shuangbao Paul Wang. Computer Memory and Storage. In Shuangbao Paul Wang, editor, *Computer Architecture and Organization: Fundamentals and Architecture Security*, pages 45–69. Springer, Singapore, 2021.
- [30] Mathworks. Support - System Requirements and Supported Compilers Previous Releases, 2023.
- [31] Mathworks. Table of Matlab release features, 2024.
- [32] R. Van De Walle, H.H. Barrett, K.J. Myers, M.I. Aitbach, B. Desplanques, A.F. Gmitro, J. Cornelis, and I. Lemahieu. Reconstruction of MR images from data acquired on a general nonregular grid by pseudoinverse calculation. *IEEE Transactions on Medical Imaging*, 19(12):1160–1167, December 2000.

- [33] James G. Pipe and Padmanabhan Menon. Sampling density compensation in MRI: Rationale and an iterative numerical solution. *Magnetic Resonance in Medicine*, 41(1):179–186, 1999. [_eprint: https://onlinelibrary.wiley.com/doi/pdf/10.1002/%28SICI%291522-2594%28199901%2941%3A1%3C179%3A%3AAID-MRM25%3E3.0.CO%3B2-V](https://onlinelibrary.wiley.com/doi/pdf/10.1002/%28SICI%291522-2594%28199901%2941%3A1%3C179%3A%3AAID-MRM25%3E3.0.CO%3B2-V).
- [34] Thomas Kirchner, Ariane Fillmer, and Anke Henning. Mechanisms of SNR and line shape improvement by B0 correction in overdiscrete MRSI reconstruction. *Magnetic Resonance in Medicine*, 77(1):44–56, January 2017.
- [35] Kangrong Zhu, Robert F. Dougherty, Hua Wu, Matthew J. Middione, Atsushi M. Takahashi, Tao Zhang, John M. Pauly, and Adam B. Kerr. Hybrid-Space SENSE Reconstruction for Simultaneous Multi-Slice MRI. *IEEE transactions on medical imaging*, 35(8):1824–1836, August 2016.
- [36] Kevin D. Harkins, Mark D. Does, and William A. Grissom. Iterative Method for Predistortion of MRI Gradient Waveforms. *IEEE Transactions on Medical Imaging*, 33(8):1641–1647, August 2014.
- [37] Martin Uecker, Peng Lai, Mark J. Murphy, Patrick Virtue, Michael Elad, John M. Pauly, Shreyas S. Vasanawala, and Michael Lustig. ESPIRiT — An Eigenvalue Approach to Autocalibrating Parallel MRI: Where SENSE meets GRAPPA. *Magnetic resonance in medicine : official journal of the Society of Magnetic Resonance in Medicine / Society of Magnetic Resonance in Medicine*, 71(3):990–1001, March 2014.
- [38] Jeremy W. Gordon, Rie B. Hansen, Peter J. Shin, Yesu Feng, Daniel B. Vigneron, and Peder E. Z. Larson. 3D hyperpolarized C-13 EPI with calibrationless parallel imaging. *Journal of Magnetic Resonance*, 289:92–99, April 2018.
- [39] P. B. Roemer, W. A. Edelstein, C. E. Hayes, S. P. Souza, and O. M. Mueller. The NMR phased array. *Magnetic Resonance in Medicine*, 16(2):192–225, 1990.
- [40] Roland Bammer, Martin Auer, Stephen L. Keeling, Michael Augustin, Lara A. Stables, Rupert W. Prokesch, Rudolf Stollberger, Michael E. Moseley, and Franz Fazekas. Diffusion tensor imaging using single-shot SENSE-EPI. *Magnetic Resonance in Medicine*, 48(1):128–136, July 2002.
- [41] Peter Kellman and Elliot R. McVeigh. Image reconstruction in SNR units: a general method for SNR measurement. *Magnetic Resonance in Medicine*, 54(6):1439–1447, December 2005.
- [42] The parallel universe: parallel imaging and novel acquisition techniques. In Donald W. McRobbie, Elizabeth A. Moore, Martin J. Graves, and Martin R. Prince, editors, *MRI from Picture to Proton*, pages 346–374. Cambridge University Press, Cambridge, 2 edition, 2006.
- [43] Elizabeth Mary Tunnicliffe, Martin John Graves, and Matthew D Robson. Use of the Noise Covariance Matrix in Array Coil Quality Assurance. In *Proceedings of the International Society for Magnetic Resonance in Medicine*, Montreal, Quebec, Canada, 2011.
- [44] Peder Eric Zufall Larson and Jeremy W. Gordon. Hyperpolarized Metabolic MRI—Acquisition, Reconstruction, and Analysis Methods. *Metabolites*, 11(6):386, June 2021. Number: 6 Publisher: Multidisciplinary Digital Publishing Institute.
- [45] Valerij G. Kiselev. Fundamentals of diffusion MRI physics. *NMR in Biomedicine*, 30(3):e3602, 2017. [_eprint: https://onlinelibrary.wiley.com/doi/pdf/10.1002/nbm.3602](https://onlinelibrary.wiley.com/doi/pdf/10.1002/nbm.3602).
- [46] Jingyuan E. Chen and Gary H. Glover. Functional Magnetic Resonance Imaging Methods. *Neuropsychology Review*, 25(3):289–313, September 2015.

- [47] Luis Hernandez-Garcia, Anish Lahiri, and Jonas Schollenberger. Recent progress in ASL. *NeuroImage*, 187:3–16, February 2019.
- [48] Yi Wei, Caiwei Yang, Hanyu Jiang, Qian Li, Feng Che, Shang Wan, Shan Yao, Feifei Gao, Tong Zhang, Jiazheng Wang, and Bin Song. Multi-nuclear magnetic resonance spectroscopy: state of the art and future directions. *Insights into Imaging*, 13(1):135, August 2022.
- [49] Thomas Campbell Arnold, Colbey W. Freeman, Brian Litt, and Joel M. Stein. Low-field MRI: Clinical promise and challenges. *Journal of Magnetic Resonance Imaging*, 57(1):25–44, 2023. [_eprint: https://onlinelibrary.wiley.com/doi/pdf/10.1002/jmri.28408](https://onlinelibrary.wiley.com/doi/pdf/10.1002/jmri.28408).
- [50] Matan Gavish and David L. Donoho. The Optimal Hard Threshold for Singular Values is $4/\sqrt{3}$. *IEEE Transactions on Information Theory*, 60(8):5040–5053, August 2014.
- [51] Javier Sánchez-González, Jeffrey Tsao, Ulrike Dydak, Manuel Desco, Peter Boesiger, and Klaas Paul Pruessmann. Minimum-norm reconstruction for sensitivity-encoded magnetic resonance spectroscopic imaging. *Magnetic Resonance in Medicine*, 55(2):287–295, February 2006.
- [52] Bertram J. Wilm, Christoph Barmet, Matteo Pavan, and Klaas P. Pruessmann. Higher order reconstruction for MRI in the presence of spatiotemporal field perturbations. *Magnetic Resonance in Medicine*, 65(6):1690–1701, 2011. [_eprint: https://onlinelibrary.wiley.com/doi/pdf/10.1002/mrm.22767](https://onlinelibrary.wiley.com/doi/pdf/10.1002/mrm.22767).
- [53] Product - Chip. URL: <https://cerebras.ai/product-chip/>. Accessed 11 Sep 2024.

10 Figure Captions

Figures

1. Diagram illustrating the composition and extension of the encoding matrix, top: Fourier Gradient Encoding, middle: Fourier Gradient Encoding with B_0 Encoding, and bottom: Fourier Gradient Encoding with Coil Sensitivity Encoding. \times indicates matrix multiplication, whilst \cdot indicates element-wise multiplication.
2. Demonstration of Pinv-Recon on a variety of k-space sampling trajectories. From left to right: Cartesian, EPI, two-fold accelerated Variable-Density Poisson Disk (VDPD), radial, spiral. From top to bottom: sampling trajectory, SVD, reconstructed Shepp-Logan image, SRF, noise matrix.
3. Illustration of Pinv-Recon’s versatility to account for multiple intertwined encoding mechanisms. From top to bottom: illustration of the encoding mechanism, SVD spectrum of general encoding matrix, reconstructed image accounting for gradient encoding only, reconstructed image accounting for all relevant encoding effects. From left to right: spiral gradient encoding + spatial off-center correction, + gradient nonlinearity correction, + B_0 off-resonance, + coil sensitivity encoding, + chemical shift encoding.
4. Comparison of MFI versus Pinv-Recon in the correction of off-resonance distortion in proton phantom and in vivo images. From top to bottom: phantom dataset, slice 5 of brain dataset, slice 7 of brain dataset. From Left to right: reference short readout time image, B_0 map, B_0 distorted image, gridding reconstructed image with MFI correction, and Pinv-Recon image with incorporated B_0 correction. Areas with distinctive differences in the two correction methods are emphasized with the blue arrow.
5. Left: Axial, coronal and sagittal views of the 3D dataset. In the middle four columns, top: varying the number of spokes used in reconstruction, middle: varying the condition number κ by changing the tSVD threshold, bottom: varying the number of iterations in images reconstructed using CG with explicit matrix vector multiplications. Right: SVD spectrum, SRF map, and noise map.
6. Top to bottom: Acceleration factors of 1 to 4. Left to right: Reconstruction using ISMRM CG-SENSE reference implementation in MATLAB, reconstruction using Pinv-Recon with coil sensitivity encoding, reconstruction using iterative CG with an explicit encoding matrix, SRF, noise map, SVD spectra.
7. Left: Reconstruction of stack-of-spirals data using gridding results in streaking artifacts, whilst Pinv-Recon eliminates these artifacts and boosts SNR, shown in original scale (top), and log scale (bottom). Right: Comparison of B_0 correction using MFI versus Pinv-Recon, with the original uncorrected image shown in the center and corrected regions-of-interest comparing both methods shown on top and bottom.
8. Comparison of different coil combination approaches in Pinv-Recon on multichannel hyperpolarized carbon-13 data. From left to right: Pyruvate, Lactate, Bicarbonate. From top to bottom: root-sum-of-squares coil combination, sensitivity-based coil combination, Pinv-Recon with coil sensitivity map included, Pinv-Recon with coil sensitivity map included reconstructed to an overdiscretized spatial grid (64×64). Mean SNR values for the first three methods are plotted in the bottom row in dotted blue, dotted red, and yellow respectively.

Tables

1. Computational times required for computing the SVD for a range of matrix sizes.
2. Results comparing B_0 correction using Pinv-Recon versus using gridding with MFI correction in a structured resolution phantom.

11 Supplementary Material Captions

1. Varying truncation threshold in solving for the reconstruction matrix in Pinv-Recon.
2. Comparison of image reconstruction metrics between Pinv-Recon (blue) and gridding (red).
3. Comparison of B_0 encoding using Pinv-Recon versus MFI B_0 correction.
4. Shepp-Logan simulations of B_0 correction using conventional MFI versus Pinv-Recon. From left to right: B_0 map, distorted images, image reconstructed with gridding and MFI, image reconstructed with Pinv-Recon.

Supplementary Material

1 Selection of SVD Truncation Threshold

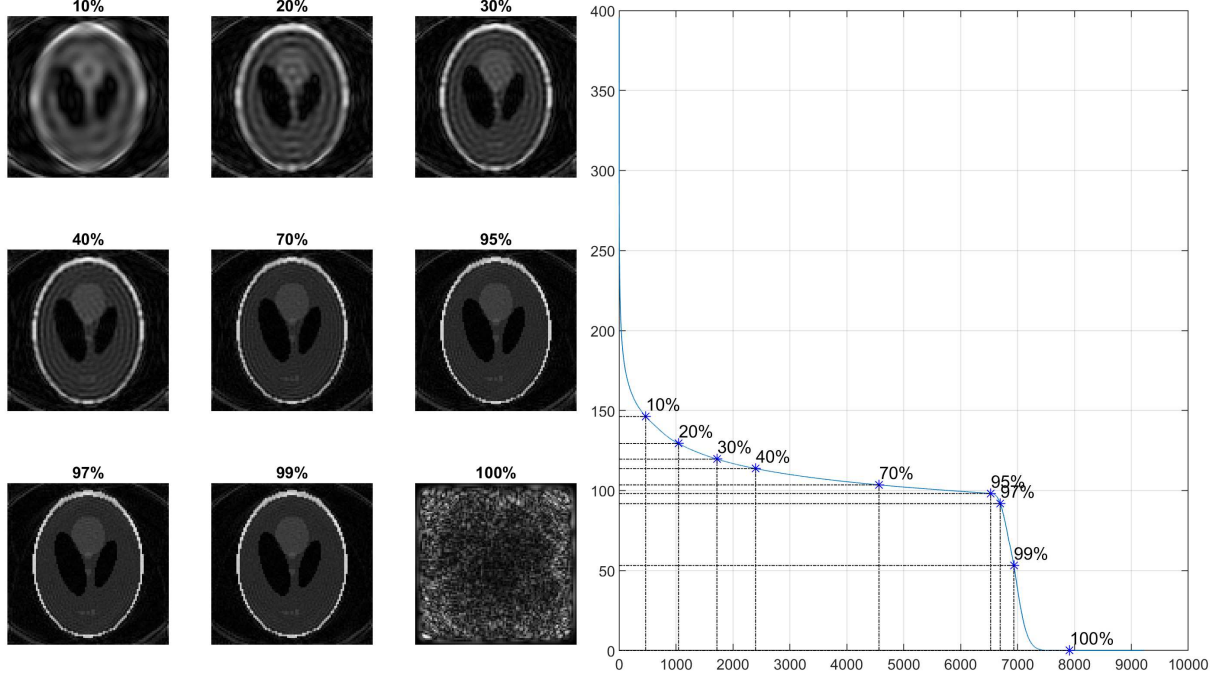


Figure 1: Varying truncation threshold in solving for the reconstruction matrix in Pinv-Recon.

Figure 1 demonstrates how the selection of different truncation thresholds affect the resulting reconstructed image. Some thresholding is required to prevent excessive noise amplification, as seen in the Shepp-Logan image reconstructed with 100% of the cumulative energy of the SVD included. However, a loss of resolution occurs when too much of the SVD is truncated.

2 Pinv versus Gridding

Pinv-Recon was compared with conventional gridding reconstruction using single-slice 2D spiral trajectories with matrix sizes (MTX) 16, 32, 64, 96, and 128. The spiral trajectories were generated using the MNS Research Pack (GE HealthCare, Munich, Germany) (Sequence parameters: maximum gradient amplitude = 30 mT/m; slew rate = 120 T/m/s; FOV = 240×240 mm; bandwidth = 250 kHz). Complex noise was added to the data with SNR from 1 to 70, with SNR defined as the ratio between signal power and noise power. Then, images were reconstructed using Pinv-Recon (with SVD truncation thresholds of 95% and 99%) and gridding. For each SNR value, 10 different noise images were generated, and the average mean squared error (MSE), peak signal-to-noise ratio (PSNR) and structural similarity index measure (SSIM) relative to the original Shepp-Logan image were computed. Masks were generated from the Shepp-Logan phantom for each matrix size to account for the circular field of view.

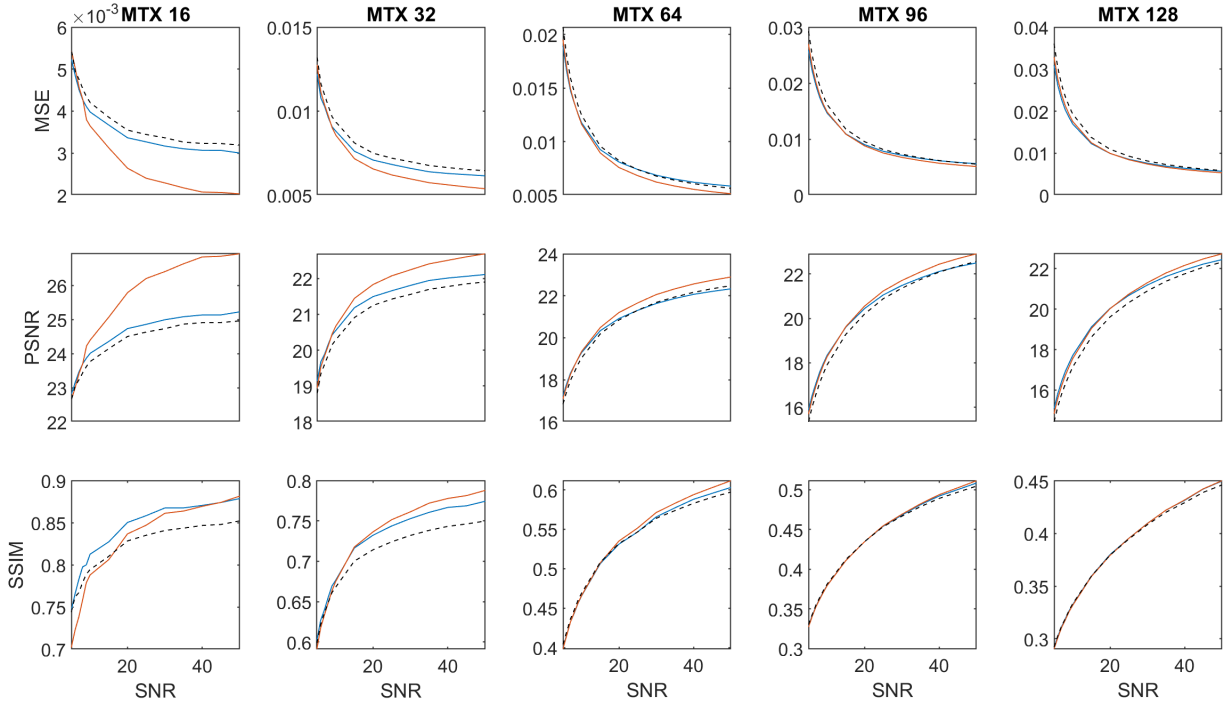


Figure 2: Comparison of image reconstruction metrics between Pinv-Recon (blue) and gridding (red).

Pinv-Recon achieves lower MSE, higher PSNR and higher SSIM compared to conventional gridding reconstruction. The improvement of Pinv-Recon is more apparent at smaller matrix sizes. At an SNR roughly above 10, a 99% SVD threshold improves the performance of Pinv-Recon. Below that, a lower SVD threshold should be selected to truncate more of the noise. Since these trajectories were generated with the same gradient and slew rate limits, the larger matrix size spirals had longer read out times.

3 Pinv with B_0 Encoding versus MFI

To further compare Pinv-Recon to conventional methods for B_0 off-resonance correction, 10 simulated B_0 maps were included in the forward encoding, according to $OffRes_{ik,ir} = \exp(j \cdot \Delta B_{0ir} \cdot t_{ik})$.

The B_0 maps were generated via random combination of solid spherical harmonics up to second order. Images at matrix sizes 16, 32, 48, and 64 were reconstructed using gridding and Pinv-Recon. For the former, B_0 correction was performed using Multifrequency Interpolation (MFI), which reconstructs an MR image to many images assuming a range of off-resonant frequencies, and then uses the B_0 map to interpolate from these images. For the latter, B_0 correction was performed by inversion of the forward encoding matrix. 50 interpolation frequencies were used for MFI to satisfy $L > \frac{4\Delta\omega_{max}T}{\pi}$, where L is the number of frequency segments, T is the readout duration and $\Delta\omega_{max}$ is the maximum off-resonance frequency.

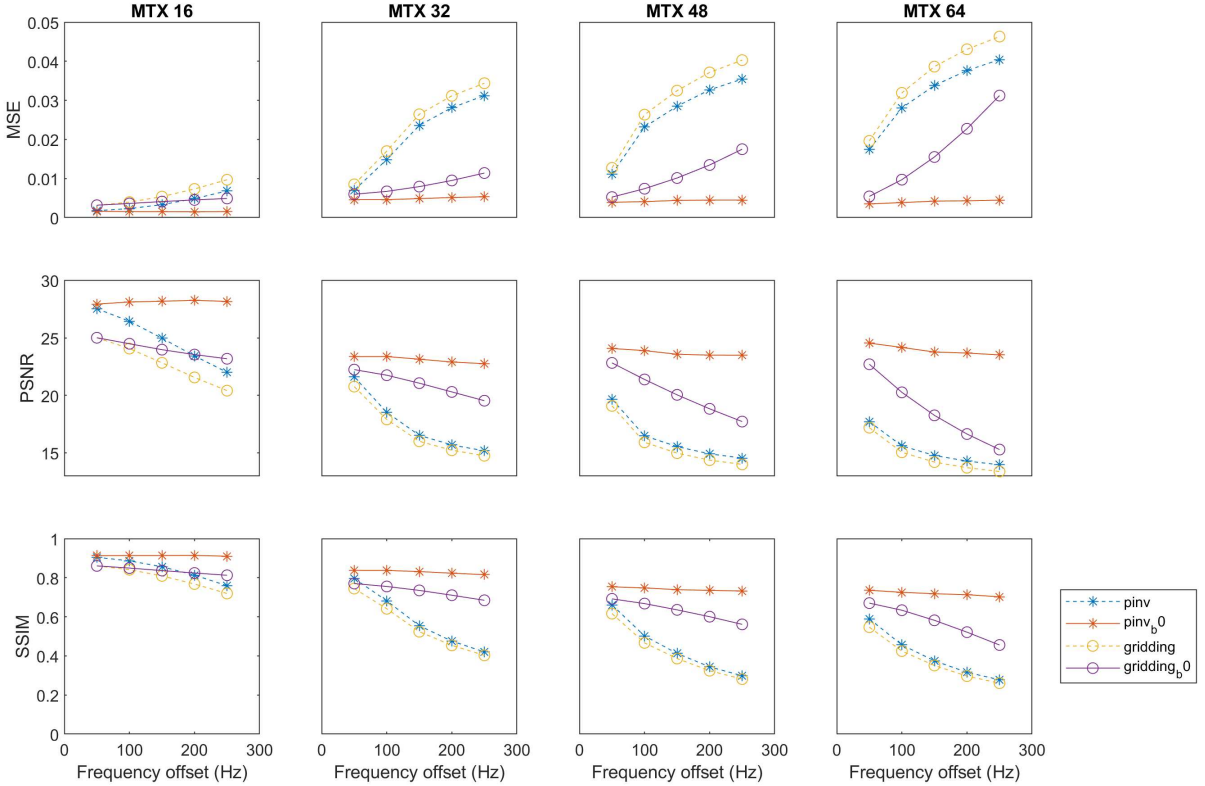


Figure 3: Comparison of B_0 encoding using Pinv-Recon versus MFI B_0 correction.

More residual B_0 distortions remain in the image reconstructed using MFI (Figure 4).

4 Details of Phantom and In Vivo Validation Acquisitions

4.1 Proton

For the 2D spiral dataset, the sequence parameters used were maximum gradient amplitude = 30 mT/m; slew rate = 120 T/m/s; FOV = 240×240 mm; bandwidth = 250 kHz. Acquisition parameters: Flip Angle = 30°; TR = minimum TR; Slice thickness = 3mm. The matrix 48 four-arm spiral was repeated at five different TEs ([0,1,2,5,10]ms) to iteratively fit for a B_0 map using the MEDI toolbox. The phantom was imaged in a 3T GE Premier scanner and using a 5-channel flexible AIR coil (GE HealthCare, WI). The healthy volunteer (Male; Age 30) was scanned in the same scanner using a 16-channel receive-only headcoil (GE HealthCare, WI), using the same single-arm MTX96 spiral and the four-arm MTX 48 spiral.

For the 3D stack-of-stars dataset, the acquisition parameters were FOV=40.0×40.0×31.68cm, resolution=1.25×1.25×2.2mm.

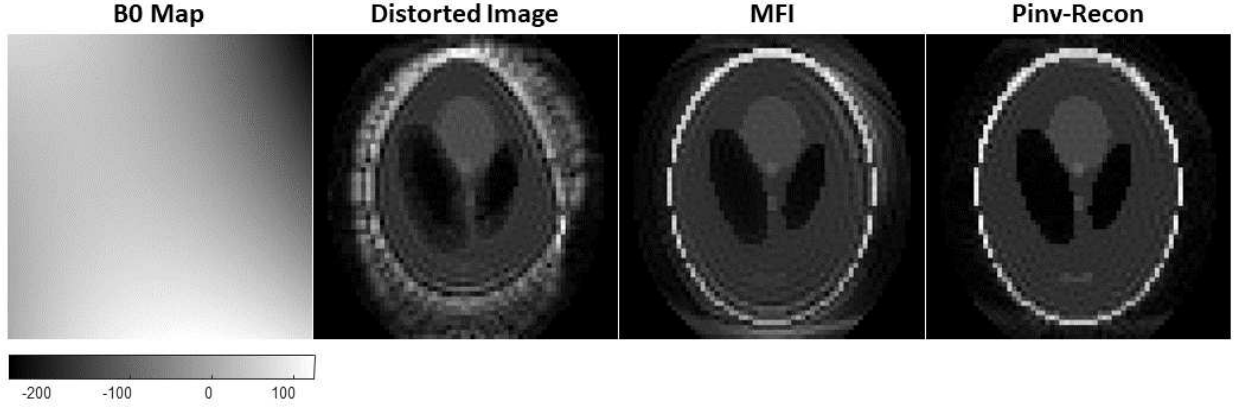


Figure 4: Shepp-Logan simulations of B_0 correction using conventional MFI versus Pinv-Recon. From left to right: B_0 map, distorted images, image reconstructed with gridding and MFI, image reconstructed with Pinv-Recon.

TE/TR=1.488/3.276ms, FA=12°, BW=±62.5kHz, interleaved fat suppression, resulting in a scan time of 5 min 58 sec.

4.2 Xenon

To acquire the stack-of-spirals dataset, the participant (Female; Age 34) inhaled 1 L hyperpolarized enriched Xenon-129 gas which was polarized for ~30 minutes. The sequence parameters were FOV = 400×400×200 mm; bandwidth = 250kHz; TR = 15.6ms; TE = 2.3ms; hard-pulse, 0.5ms; effective flip angle per volume = 66° (3° per excitation).

The low resolution 2D spiral was integrated into the Transmit Gain Calibration scan of another participant, and only used a 10% dose of Xenon. The participant (Female; Age 24) inhaled 1 L hyperpolarized gas containing a mixture of xenon, polarized for ~10 min, and nitrogen (0.1:0.9 L, respectively). FOV= 400×400 mm, 1.8 ms partially self-refocused excitation pulse, TR = 230 ms, bandwidth = 250 kHz. The B_0 map was determined by repeating this acquisition at echo times of 1.4, 2.3, 3.9, 6.5, 10.8, 18, 30, 50ms then fitting with the MEDI toolbox.

For both datasets, participants were imaged in a 3T GE Premier MRI scanner (GE Healthcare, WI) with a flexible Tx/Rx ^{129}Xe wrap-around coil (PulseTeq, Chobham, UK). Enriched ^{129}Xe was polarized using a commercial polarizer (Polarean, Durham, NC, USA). Center frequency (f_0) was determined with respect to the water peak.

4.3 Carbon

The volunteer was scanned after intravenous injection of 35 mL of 250 mM hyperpolarized [1- ^{13}C]pyruvate following polarization for ~4 hours in a SPINLab hyperpolarizer (GE Healthcare, WI), with a resulting polarization of ~25%. Transmit gain (TG) for ^{13}C was calibrated using a thermal ^{13}C urea phantom placed by the participant's head. The spectral-spatial single-arm spiral sequence had 240×240 mm FOV and eight 20 mm slices with pyruvate ($FA_{py} = 5^\circ$), lactate ($FA_{lac} = 15^\circ$), and bicarbonate ($FA_{bic} = 60^\circ$) maps acquired at ~4 second intervals. The patient was scanned using a GE Premier system with an 8-channel transmit-receive ^{13}C / ^1H headcoil (Rapid Biomedical, Rimpär).